143
9-24-81

ornl

OAK
RIDGE
NATIONAL
LABORATORY

UNION
CARBIDE

OPERATED BY
UNION CARBIDE CORPORATION
FOR THE UNITED STATES
DEPARTMENT OF ENERGY

Dr. 3047
B7304

ORNL/TM-7878

MASTER

# Calculated Neutron and Gamma-Ray Energy Spectra from 14-MeV Neutrons Streaming Through an Iron Duct: Comparison with Experiment

R. T. Santoro
R. G. Alsmiller, Jr.
J. M. Barnes
G. T. Chapman
J. S. Tang

ORNL/TM-7878
Dist. Category UC-20d

Contract No. W-7405-eng-26

Engineering Physics Division



# Calculated Neutron and Gamma-Ray Energy Spectra From 14-MeV Neutrons Streaming Through an Iron Duct: Comparison With Experiment*

R. T. Santoro
R. G. Alsmiller, Jr.
J. M. Barnes+
G. T. Chapman
J. S. Tang+

*Submitted for
Journal publication

+UCC-ND Computer Sciences Division

Date Published - September 1981

This Work Sponsored by
Department of Energy
Office of Fusion Energy

OAK RIDGE NATIONAL LABORATORY
Oak Ridge, Tennessee 37830
operated by
UNION CARBIDE CORPORATION
for the
DEPARTMENT OF ENERGY

## ACKNOWLEDGEMENTS

The authors wish to thank R. A. Lillie, R. L. Childs and R. W. Peelle for their suggestions and comments throughout this work. We are also grateful to D. C. Larson and R. A. Lillie for reviewing the manuscript.

TABLE OF CONTENTS

## ABSTRACT

Integral experiments that measure the streaming of ∿14 MeV neutrons through a 0.30-m-diameter iron duct (L/D ∿3) imbedded in a concrete shield have been carried out at the Oak Ridge National Laboratory. Calculated and measured neutron and gamma-ray energy spectra are compared at sixteen detector locations on and off the cylindrical axis of the duct. The measured spectra were obtained using an NE-213 liquid scintillator detector with pulse-shape discrimination to simultaneously resolve neutron and gamma ray events. The calculated spectra were obtained using a computer code network that incorporates two radiation transport methods: discrete ordinates (with $P_3$ multigroup cross sections) and Monte Carlo (with continuous-point cross sections). The two radiation transport methodologies are required to properly account for neutrons that single scatter from the duct to the detector. The calculated and measured outgoing neutron energy spectra above 850 keV agree within 5-50% depending on detector location and neutron energy. The calculated and measured gamma ray spectra above 750 keV are also in favorable agreement, ∿5-50%, depending on detector location and gamma ray energy.

# I. INTRODUCTION

To accurately perform radiation transport calculations of neutrons and gamma rays streaming through the ducts and other penetrations in the blanket-shield assembly of a fusion reactor, it is necessary to have experimental data against which the results of calculations may be compared. Numerous analytic studies have been made to estimate the impact of radiation streaming on fusion reactors and reactor component performance,[1-7] but because there are no operating, neutron producing reactors in existence, there are no measured data available for verifying the results of the calculations.

Fusion reactors will contain numerous ducts and other penetrations in the blanket-shield assembly. These ducts are required for the essential functions of vacuum pumping, rf and neutral beam heating, diagnostics, etc. The ~14 MeV neutrons produced from DT reactions in the plasma, along with low-energy neutrons and gamma rays produced from the reactions of these neutrons in the materials surrounding the plasma and in the duct, will stream out of the duct and give rise to an excess radiation field in an otherwise adequately shielded environment. This excess radiation will increase radiation damage, nuclear heating, and neutron induced activation rates in vital components such as insulators, cryogenic systems, and electronic instrumentation to the extent that replacement and maintenance requirements will be considerably different than that anticipated if these components were in a shielded environment. The higher heating rates in cryogenic equipment, for example, will result in higher operating and capital costs because of increased refrigeration requirements.

Radiation streaming is one of the more serious problems to be resolved in fusion reactor design so it is important, therefore, that experimental data be obtained to verify the radiation transport methods and the nuclear data that are being used in the analysis of these types of problems. A series of integral measurements are underway at the Oak Ridge National Laboratory to obtain measured data from ∿14-MeV neutrons streaming through ducts having characteristics typical of those found in fusion reactors.

In this paper measured and calculated neutron and gamma ray energy spectra produced by the streaming of ∿14-MeV neutrons are compared as a function of position relative to the mouth of a 0.30-m-diameter iron duct having a length-to-diameter (L/D) ratio of ≃ 3. The ∿14-MeV neutrons are produced from the reactions of 250-keV deuterons in a tritium target. The spectra are compared at sixteen detector locations on and off the duct axis and at several distances from the mouth of the duct. The composition and the dimensions of the duct are representative of those found in fusion reactor blankets and shields, but the duct geometry is in no way a mockup of an actual penetration in a reactor blanket-shield assembly. The purpose of this study is to identify problems that will arise in the analysis of radiation streaming through penetrations. This work is an extension of measurements and calculations that have been reported previously of the transport of ∿14-MeV neutrons through materials typical of those found in fusion reactor shields[8] and is the first in a series of streaming experiments that will proceed from simple duct geometries to more "prototypic" configurations.

A description of the experimental facility and the experimental procedures is given in Section II. The details of the calculations including the calculational model, radiation transport methods, and nuclear data are given in Section III. The calculated and measured neutron and gamma ray energy spectra are compared and discussed in Section IV.

## II. DETAILS OF THE EXPERIMENT

The experimental facility used for carrying out the integral measurements of ∿14-MeV neutrons streaming through an iron duct imbedded in a concrete shield is shown in an artist's rendition in Fig. 1. An electrostatic generator is used to accelerate deuterons to a kinetic energy of 250 keV. The deuterons are directed through a drift tube and focused onto a 4 mg/cm$^2$-thick titanium-tritide target wherein ∿14-MeV neutrons are produced in the

$$D + T \rightarrow n + {}^4He + 17.36 \text{ MeV} \qquad (1)$$

fusion reaction. The tritium target is enclosed in a cylindrical, re-entrant, iron can having an inner diameter of 0.30 m and a wall thickness of 0.075 m. The iron source can is enclosed in a concrete structure that serves both as a shield and as an experiment support. The iron duct through which the neutrons stream is encased in a 0.78-m-thick concrete block which is mounted in the cavity in the concrete shield-support structure. The iron duct forms an extension of the source can. The inner diameter of the duct is 0.30 m and it has a wall thickness of 0.075 m. The duct extends 0.85 m from the tritium target (neutron source) and the

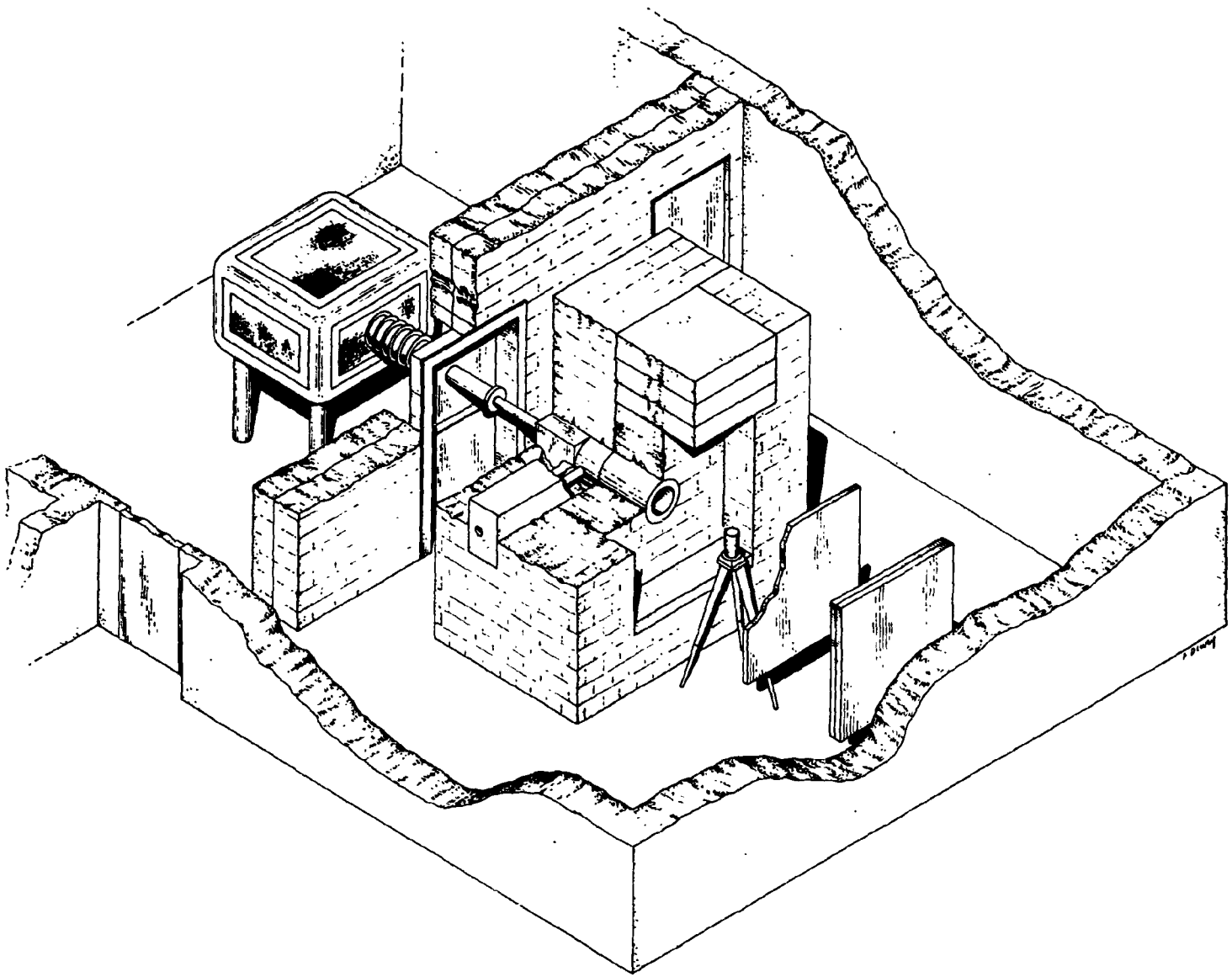


Fig. 1. An artist's rendition of the experimental facility.

length-to-diameter (L/D) ratio of the duct is 2.83. The L/D ratio is measured from the tritium target to the mouth of the duct.

The iron source can was carefully designed to shape the neutron spectrum exiting the can and to reflect neutrons emitted in the backward direction.[9] The spectrum is similar to that which will exist at the first wall of a fusion reactor and is characterized by a ∿14-MeV neutron peak and a low-energy neutron tail. In the reactor, the low-energy neutron component arises from elastic and inelastic scattering reactions of the source neutrons in the materials that surround the plasma.

The concrete shield-support structure has a thickness of ∿1 m in all directions perpendicular to the deuteron beam-target axis. It is effective as a biological shield and for reducing neutron and gamma ray background radiation levels in the vicinity of the detector. A detailed analytic study was carried out to optimize the shield-support dimensions and composition to minimize the radiation leakage and reduce the scattered radiation from the experiment room walls. A detailed discussion of the analytic procedures and the results of these calculations may be found in Ref. 9.

Also shown in Fig. 1 are a series of plates between the detector and the room wall. It was revealed in the calculations in Ref. 9 that a significant contribution to the background occurred from thermal neutrons emanating from the concrete wall. The stainless-steel plates placed between the detector and the wall reduces the thermal neutron flux at the detector.

The neutron-gamma-ray-detector consisted of 66.1 g of NE-213 liquid scintillator contained in a cylindrical aluminum can having a wall thickness of $4.3 \times 10^{-4}$ m and coated on the inside with titanium oxide paint to increase light reflection.

The active volume of the detector is $7.9 \times 10^{-5}$ $m^3$ (0.047 m dia. x 0.047 m high). The scintillator was mounted on a RCA 8850 photomultiplier tube. Neutron and gamma ray events in the detector were separated using pulse-shape discrimination methods and stored in separate memory locations in a PDP-11 pulse-height analyzer/computer. The pulse-height data were permanently stored on magnetic disks. The neutron and gamma ray data were normalized to the absolute neutron yield from the target which was determined using the associated particle method.

The neutrons produced from the interactions of 250-keV deuterons with tritium are emitted isotropically in the center-of-mass system. The alpha particles produced in the reaction are emitted at 180° with respect to the neutron. If the alpha particles are detected and counted within a well-defined solid angle, the number of conjugate neutrons is known and the total neutron source strength can be determined from the kinematics of the reaction.

The pulse-height data were obtained for neutrons with energies above 850 keV. The dynamic range of the neutron pulse-height distribution and the nonlinearity of the light output from the scintillator restricts the detection of neutrons to those with energies above 850 keV. The gamma ray pulse-height was biased for energies above 750 keV even though a somewhat broader energy range is possible since the response of NE-213 is linear for gamma rays. The neutron and gamma ray pulse-height spectra were unfolded using the program FERD[10] to produce energy spectra. The neutron response matrix was obtained using the pulsed neutron beam from the Oak Ridge Linear Accelerator[11] and the gamma ray response matrix was generated using gamma ray sources of known energies. The energy resolution

of the detector varies as

$$R_n = \sqrt{300 + 800/E_n} \qquad (2)$$

for neutrons of energy $E_n$ and as

$$R_\gamma = \sqrt{170 + 288/E_\gamma} \qquad (3)$$

for gamma rays of energy $E_\gamma$, where $R_n$ and $R_\gamma$ are the full width-at-half-maximum (in percent) of the detector response to neutrons or gamma rays, respectively.

Additional details of the experimental facility, electronic instrumentation, detector, and data processing may be found in Refs. 11 and 12.

## III. DETAILS OF THE CALCULATIONS

The calculated energy spectra were obtained using the two-dimensional representation of the experimental room and components shown in Fig. 2. The concrete shield-experiment support structure, the iron duct concrete shield assembly, the detectors, and the thermal shield and room walls were modeled in r-z cylindrical geometry with symmetry about the deuteron beam axis. The experimental components shown in Fig. 2 are modeled in a reduced geometry. That is, the walls and ceiling are replaced in the model by an albedo surface at the radial boundary of the model. The validity of incorporating albedo surfaces at this boundary and the rationale for reducing the geometry are discussed in Ref. 9. In this reference, it was concluded that a reflection factor of 20% for neutrons and gamma rays of all energies reproduced the scalar flux profiles in the vicinity of the detector locations in the reduced geometry compared to those obtained using a cylindrical model of the full room. The principal advantages for compressing the

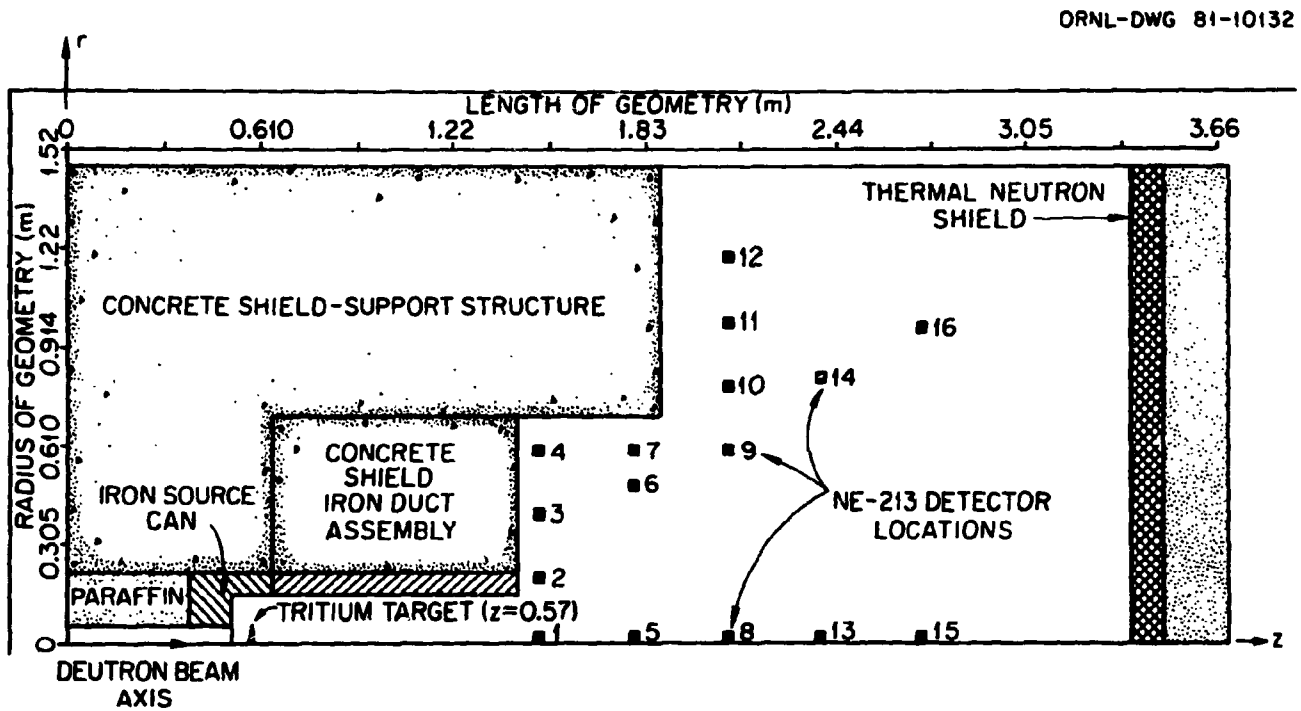


Fig. 2. Two-dimensional calculational model of the experimental configuration.

geometry are the smaller number of mesh intervals to describe the experiment, the smaller computer core size, and shorter transport code running time. The two-dimensional representation of the experimental facility was modeled using 62 radial and 87 axial mesh intervals to describe the components.

The detector locations at which the neutron and gamma ray energy spectra were measured and calculated are also shown in Fig. 2. Data were obtained at five detector locations on the axis and at eleven positions off the axis of symmetry.

In the experiment, the detector locations were specified in a right-hand coordinate system with the z-axis corresponding to the deuteron beam axis and with the x-axis parallel to the experiment room floor. The off-axis measurements were made with the detectors displaced along the positive x-axis. To assure that the measured data were symmetric about the z-axis and to validate the use of two-dimensional calculational procedures, some neutron and gamma ray spectra were also measured for detector locations along the negative x-axis and the positive y-axis. The measured spectra were in excellent agreement for positive and negative displacement of the detector along the x-axis and positive displacements of the detector along the y-axis.

The r-z coordinates of the detector positions used in the calculations and shown in Fig. 2 are given in Table I. The z coordinate is the distance from the origin of the coordinates of calculational model to the center of the detector and the r coordinate is the distance measured radially from the z axis to the center of the detector (see Fig. 2). The axial distance from the source to the detector may be found by subtracting 0.57 m from the z values given in Table I.

Table I. Detector Coordinates

| Detector Number* | Detector Coordinates (m) | |
|---|---|---|
| | r | z |
| 1 | 0.0 | 1.51 |
| 2 | 0.19 | 1.51 |
| 3 | 0.39 | 1.51 |
| 4 | 0.59 | 1.51 |
| 5 | 0.0 | 1.78 |
| 6 | 0.47 | 1.78 |
| 7 | 0.59 | 1.78 |
| 8 | 0.0 | 2.08 |
| 9 | 0.59 | 2.08 |
| 10 | 0.79 | 2.08 |
| 11 | 0.98 | 2.08 |
| 12 | 1.19 | 2.08 |
| 13 | 0.0 | 2.38 |
| 14 | 0.81 | 2.38 |
| 15 | 0.0 | 2.70 |
| 16 | 0.98 | 2.70 |

The neutron and gamma ray energy spectra were calculated using a computer code network that incorporates both discrete ordinates and Monte Carlo radiation transport methods. The sequence of calculations attempts to account for the physical processes that occur in the experiment as well as the nonphysical anomalies (e.g., ray effects, etc.) that are introduced by the radiation transport methods.

The energy distribution of neutrons produced in the reactions of 250 keV deuterons in the 4 $mg/cm^2$-thick titanium-tritide target varies by $\sim$14% in the angular interval between 0° and 180°. This angle-energy dependence must be taken into account in the radiation transport calculations to insure that the measured and calculated spectra are compared to the same neutron source distribution. The probability, P, that a deuteron of energy $E_d$ reacts while traveling a distance dx in a target containing $N_t$ tritium atoms per $cm^3$ is

$$P = N_t \int_0^{E_d} \sigma(E)dE/(dE/dx) \qquad (4)$$

where $\sigma(E)$ is the microscopic cross section for the $T(D,n)^4He$ reaction and dE/dx is the stopping power for deuterons in titanium-tritide. If $\sigma(E)$ is expressed as the angular differential cross section for the reaction, then P is the probability for the emission of a neutron into any solid angle. Equation (4) can be solved to yield the neutron emission probabilities at all deuteron energies and for all angles into which the neutron is emitted. The energies of the emitted neutrons are obtained as a function of the deuteron energy and polar angle of emission from the kinematic equations for a two-body reaction. The probabilities for the

emission of neutrons from the tritium target into the polar angular intervals of 0-10, 10-40, 40-90, and 90-180 degrees (measured with respect to the deuteron-target axis) are given as a function of neutron energy in Table II.* The angular intervals were selected on the basis of the iron duct and source can geometries. The angular interval of 0-10 degrees corresponds to the angle at which neutrons are emitted directly out of the iron duct. That is, the polar angle defined by a ray from the D-T source to the rim of the duct is 10 degrees. The 10-40 degree angular interval defines the angles at which neutrons are emitted directly out of the source can in the absence of the duct. The angular intervals of 40-90 and 90-180 degrees define the angles of neutron emission into the lateral surface and the rear of the source can, respectively. These data serve as the source term in the radiation transport codes.

The sequence of radiation transport calculations that was used to obtain the neutron and gamma ray energy spectra is shown in Fig. 3. The calculational sequence incorporates both discrete ordinates (with multigroup formatted cross section data) and Monte Carlo (with continuous cross section data) radiation transport methods. The necessity for using both radiation transport methods arose when it was determined that using only discrete ordinates methods yielded neutron spectra that were in poor agreement with the measured data. The poor agreement was due to the inadequacy of the $P_3$ Legendre expansion of the multigroup neutron scattering cross sections in predicting the single scattering of high energy (>10 MeV)

---

*The energy intervals correspond to the energy boundaries of the multigroup structure used to describe the transport cross sections.

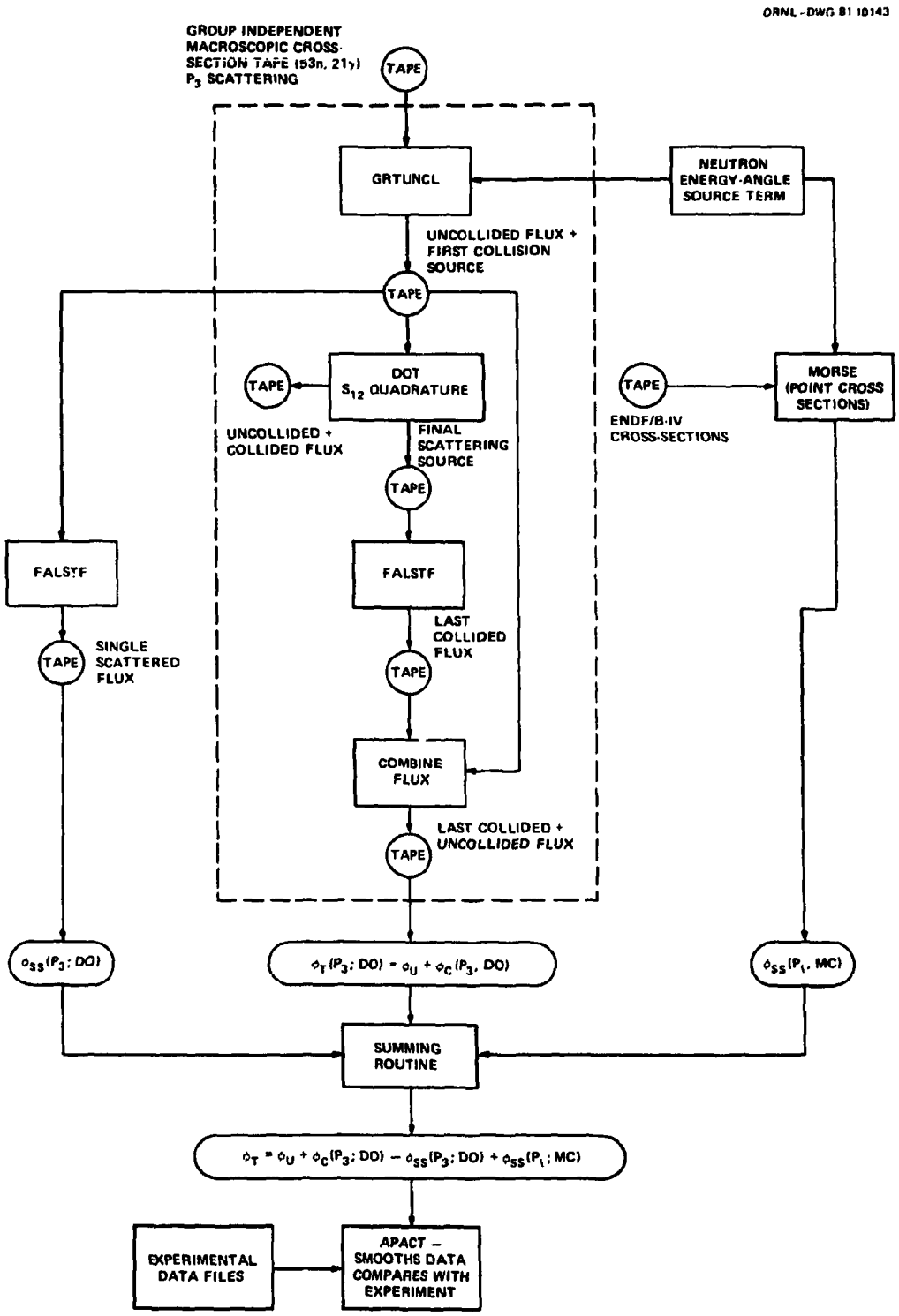


Fig. 3. Sequence of calculations used to obtain the neutron and gamma ray energy spectra.

Table II. Angle-Energy Dependence of Neutrons From the $T(D,n)^4He$ Reaction

| Energy Interval (MeV) | Angular Interval 0°-10° | 10°-40° | 40°-90° | 90°-180° |
|---|---|---|---|---|
| 14.92-15.68 | 0.0016 | 0.0014 | | |
| 14.55-14.92 | 0.0042 | 0.0866 | 0.0697 | |
| 14.19-14.55 | 0.0006 | 0.0164 | 0.2460 | |
| 13.80-14.19 | | | 0.0750 | 0.2163 |
| 13.50-13.80 | | | | 0.2080 |
| 12.84-13.50 | | | | 0.0642 |
| | 0.0064 | 0.1144 | 0.3907 | 0.4885 |

neutrons from the iron duct to the off-axis detectors. The continuous (point) cross-section data describe the neutron scattering using high order ($\ell \gg 7$) Legendre coefficients and these are used in the Monte Carlo analysis to more accurately describe the single scattering of the neutrons from the duct.

However, before proceeding with the discussion of the treatment of the calculation of neutron single scattering, it is prudent to describe the cross section data that are used in the discrete ordinates segment of the calculational sequence. These radiation transport calculations were carried out using a 53-neutron, 21-gamma-ray multigroup cross section library obtained by collapsing the 171-neutron, 36-gamma-ray VITAMIN C data library (ENDF/B-IV).[13] The VITAMIN C library was created as a general purpose cross section data set for the analysis of fusion neutronics problems.

The library contains cross section data for sixty elements that have been proposed for use in both fusion and hybrid fusion/fission systems. In this library neutron scattering is approximated using a $P_3$ Legendre series expansion.

The fine group library was collapsed using the ANISN code[14] by representing the experimental components in the angular intervals given in Table II in spherical geometry and using the neutron emission probability in that angular interval as the weighting function. The energy boundaries of the broad group library, given in Table III, were based in part on those used in the DLC-47 cross section library,[15] but expanded at high energies so that the DT neutron source energy distribution could be more accurately represented in the transport calculations. The VITAMIN C data were initially processed using BONAMI2 module of the AMPX[16] code system to self-shield the nuclides. The composition of the materials used in the calculations is given in Table IV.

The sequence of discrete radiation transport calculations that were initially used to obtain the neutron and gamma ray energy spectra is shown in the central portion of Fig. 3 and enclosed by the dashed lines. The calculation is initiated using the GRTUNCL code[17] to obtain the first collision source and uncollided neutron flux distribution at all spatial mesh intervals in the calculational geometry. The neutron source term given in Table II serves as the input to the GRTUNCL code. The neutron source is defined in terms of the direction cosines and the neutron intensity. However, the GRTUNCL code assumes isotropic neutron emission from a point source. To account for the anisotropy of the DT neutrons, the neutron energy-angle probabilities, $P(\Delta E,\Delta\Theta)$, from Table II were

Table III. 53-Neutron, 21-Gamma-Ray Energy Radiation Transport Cross Section Group Structure

| Neutron Group | Upper Energy (eV) | Neutron Group | Upper Energy (eV) | Gamma Ray Group | | Upper Energy (MeV) |
|---|---|---|---|---|---|---|
| 1 | 0.17333E + 08 | 28 | 0.60810E + 06 | 54 | 1 | 14.0 |
| 2 | 0.15683E + 08 | 29 | 0.49787E + 06 | 55 | 2 | 12.0 |
| 3 | 0.14918E + 08 | 30 | 0.36883E + 06 | 56 | 3 | 10.0 |
| 4 | 0.14550E + 08 | 31 | 0.29850E + 06 | 57 | 4 | 8.0 |
| 5 | 0.14191E + 08 | 32 | 0.29720E + 06 | 58 | 5 | 7.5 |
| 6 | 0.13840E + 08 | 33 | 0.18316E + 06 | 59 | 6 | 7.0 |
| 7 | 0.13499E + 08 | 34 | 0.11109E + 06 | 60 | 7 | 6.5 |
| 8 | 0.12840E + 08 | 35 | 0.67379E + 05 | 61 | 8 | 6.0 |
| 9 | 0.12214E + 08 | 36 | 0.40868E + 05 | 62 | 9 | 5.5 |
| 10 | 0.11052E + 08 | 37 | 0.24788E + 05 | 63 | 10 | 5.0 |
| 11 | 0.10000E + 08 | 38 | 0.23579E + 05 | 64 | 11 | 4.5 |
| 12 | 0.90484E + 07 | 39 | 0.15034E + 05 | 65 | 12 | 4.0 |
| 13 | 0.81873E + 07 | 40 | 0.91188E + 04 | 66 | 13 | 3.5 |
| 14 | 0.74082E + 07 | 41 | 0.55308E + 04 | 67 | 14 | 3.0 |
| 15 | 0.60653E + 07 | 42 | 0.33546E + 04 | 68 | 15 | 2.5 |
| 16 | 0.49659E + 07 | 43 | 0.20347E + 04 | 69 | 16 | 2.0 |
| 17 | 0.40657E + 07 | 44 | 0.12341E + 04 | 70 | 17 | 1.50 |
| 18 | 0.36788E + 07 | 45 | 0.74852E + 03 | 71 | 18 | 1.0 |
| 19 | 0.27253E + 07 | 46 | 0.45400E + 03 | 72 | 19 | 0.60 |
| 20 | 0.23653E + 07 | 47 | 0.27536E + 03 | 73 | 20 | 0.20 |
| 21 | 0.23069E + 07 | 48 | 0.16702E + 03 | 74 | 21 | 0.10 |
| 22 | 0.22313E + 07 | 49 | 0.10130E + 03 | | | 0.010 |
| 23 | 0.16530E + 07 | 50 | 0.61442E + 02 | | | |
| 24 | 0.13534E + 07 | 51 | 0.37267E + 02 | | | |
| 25 | 0.86294E + 06 | 52 | 0.10677E + 02 | | | |
| 26 | 0.82085E + 06 | 53 | 0.41399E + 00 | | | |
| 27 | 0.74274E + 06 | | 0.10000E - 04 | | | |

Table IV. Composition of Materials

| Element | Composition (Atom/cm·Barn) | | | |
|---|---|---|---|---|
| | Concrete | Air | Iron | SS-304 |
| H | 7.86-3* | | | |
| N | | 3.64-5 | | |
| O | 4.39-2 | 9.74-6 | | |
| Na | 1.05-3 | | | |
| Mg | 1.40-4 | | | |
| Al | 2.39-3 | | | |
| Si | 1.58-2 | | | |
| K | 6.90-4 | | | |
| Ca | 2.92-3 | | | |
| Cr | | | | 1.77-2 |
| Mn | | | | 1.77-3 |
| Fe | 3.10-4 | | 8.48-2 | 6.02-2 |
| Ni | | | | 7.83-3 |

*Read as $7.86 \times 10^{-3}$

integrated using a solid angle factor given by

$$P_W(\Delta E,\Delta\Theta) = \frac{2P(\Delta E,\Delta\Theta)}{\int_{\Theta_1}^{\Theta_2} \sin\Theta' d\Theta'} \qquad (5)$$

where $P_W(\Delta E,\Delta\Theta)$ is the solid angle weighted probability for neutrons in the energy interval $\Delta E$ emitted into the angular interval $\Delta\Theta$ and $\Theta$ is the angle measured relative to the deuteron-target axis.

The first collision source from GRTUNCL is the input to the two-dimensional discrete ordinates code DOT.[18] This code calculates the collided flux distributions using the first collision data as a spatially distributed source. The calculation is carried out using an $S_{12}$ angular quadrature. A final scattering source tape is generated in DOT and is employed to carry out a last-flight transport calculation using the FALSTF code[19] to obtain the neutron and gamma ray energy dependent flux at each detector location. The output from FALSTF is combined with the uncollided flux from GRTUNCL to yield the total flux at each detector location.

The differential neutron energy spectra calculated using the discrete ordinates segment of the radiation transport code network are compared with the measured neutron energy spectra in Figs. 4-8. The data are presented in order of increasing axial displacement of the detector and, in each figure, as a function of increasing radial displacement (from top to bottom in the figure) for a fixed axial position. The solid curves are the measured spectra and the points show the calculated results. The two solid curves shown for each detector location represent a 68% confidence interval in the measured spectra that is introduced by the unfolding procedure[10] used to resolve the neutron spectra from the pulse-height

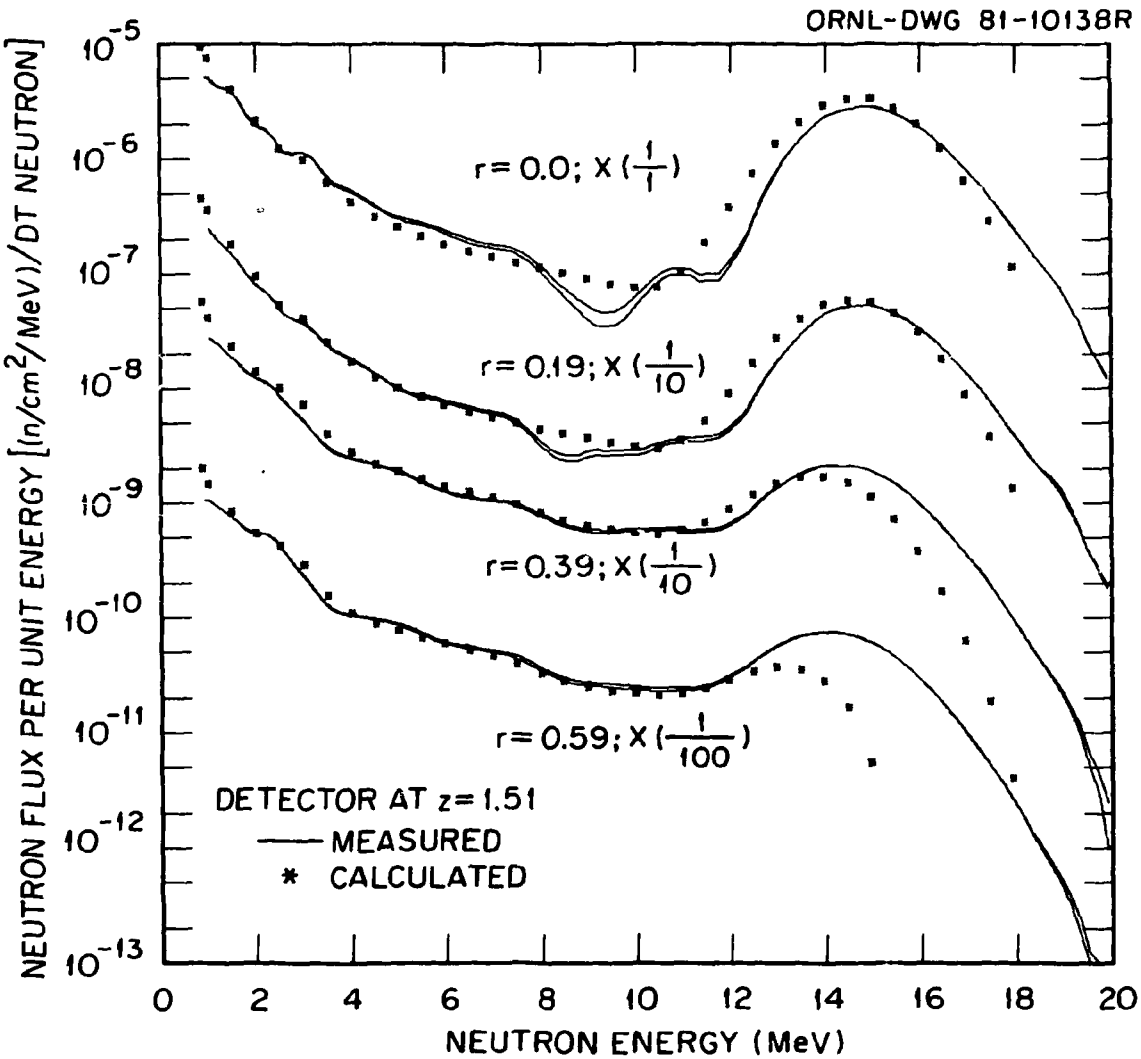


Fig. 4. Neutron flux per unit energy versus neutron energy for the detectors z = 1.51 m; r = 0.0, 0.19, 0.39, and 0.59 m. The calculated data were obtained using discrete ordinates radiation transport methods.

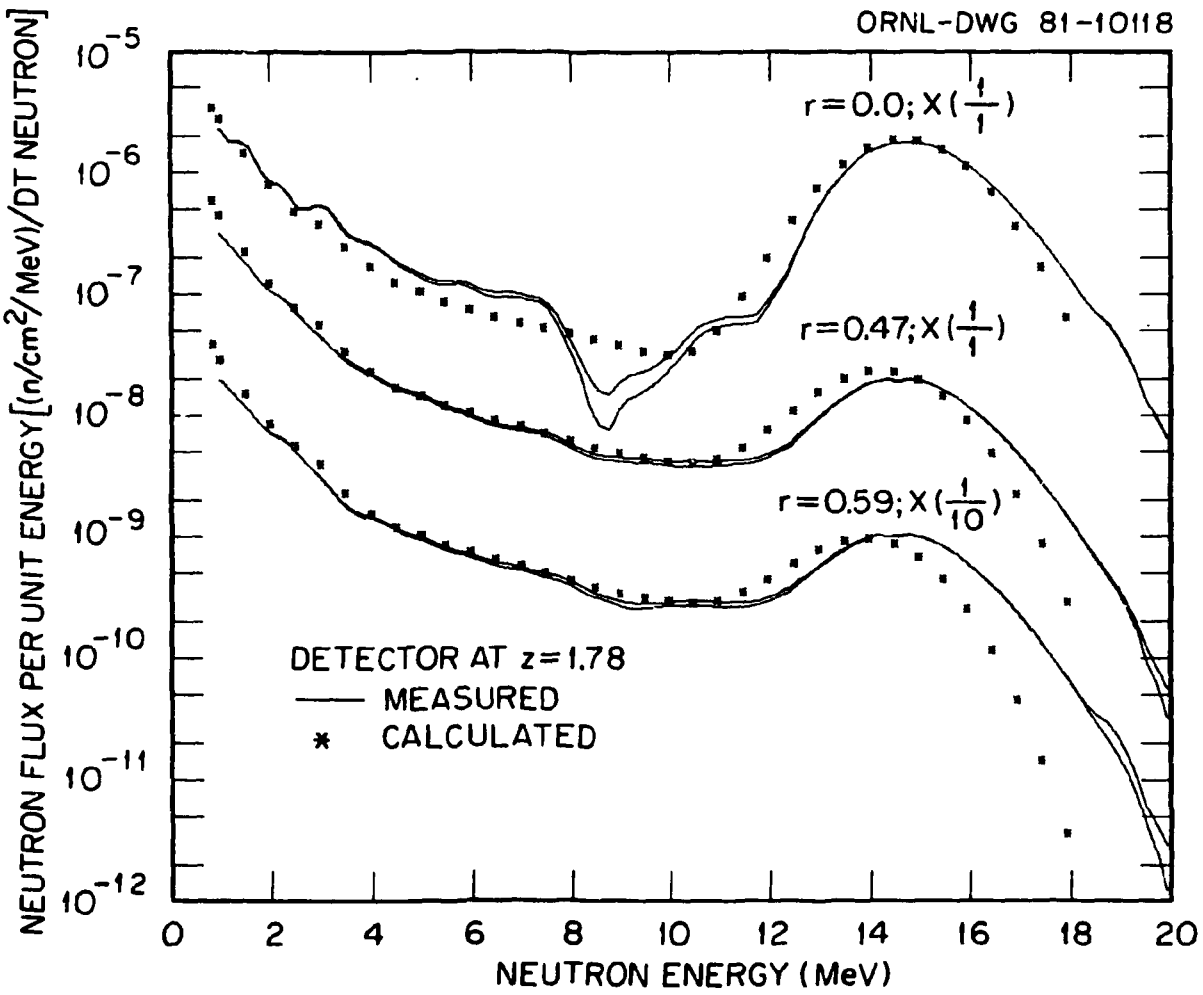


Fig. 5. Neutron flux per unit energy versus neutron energy for the detectors at z = 1.78 m; r = 0.0, 0.47, and 0.59 m. The calculated data were obtained using discrete ordinates radiation transport methods.

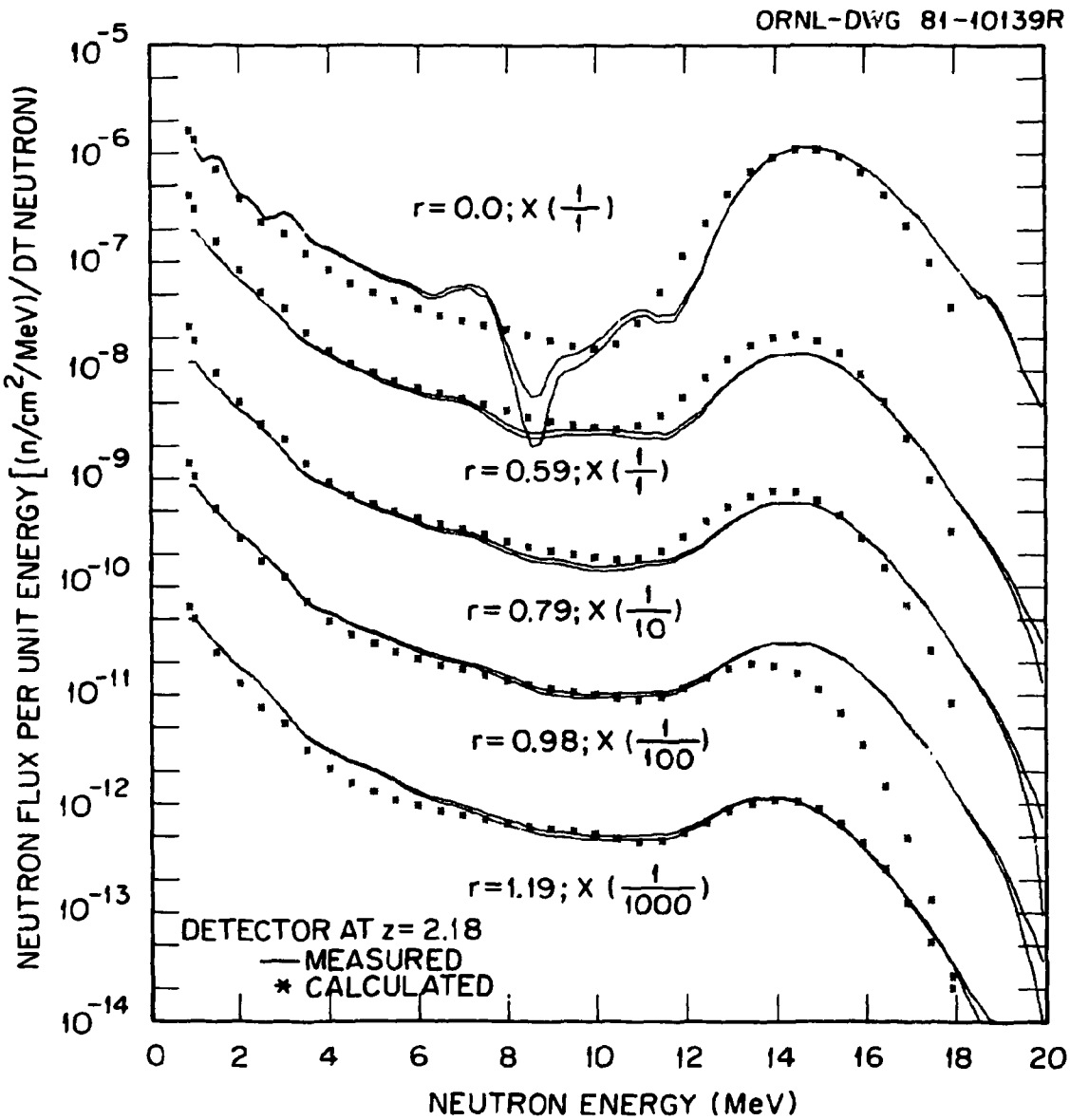


Fig. 6. Neutron flux per unit energy versus neutron energy for the detectors at z = 2.08 m; r = 0.0, 0.59, 0.79, 0.98, and 1.19 m. The calculated data were obtained using discrete ordinates radiation transport methods.

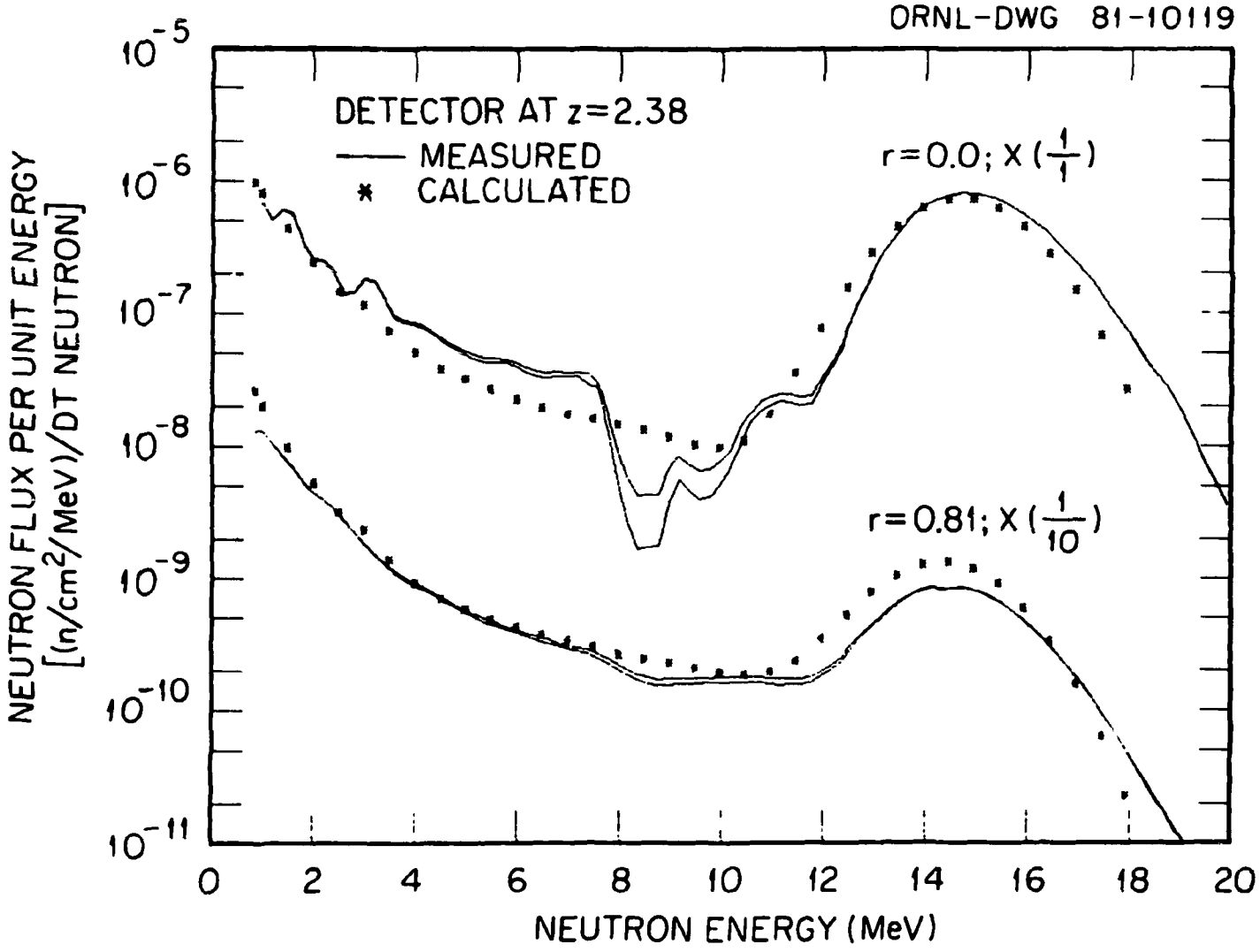


Fig. 7. Neutron flux per unit energy versus neutron energy for the detectors at z = 2.38 m; r = 0.0 and 0.81 m. The calculated data were obtained using discrete ordinates radiation transport methods.

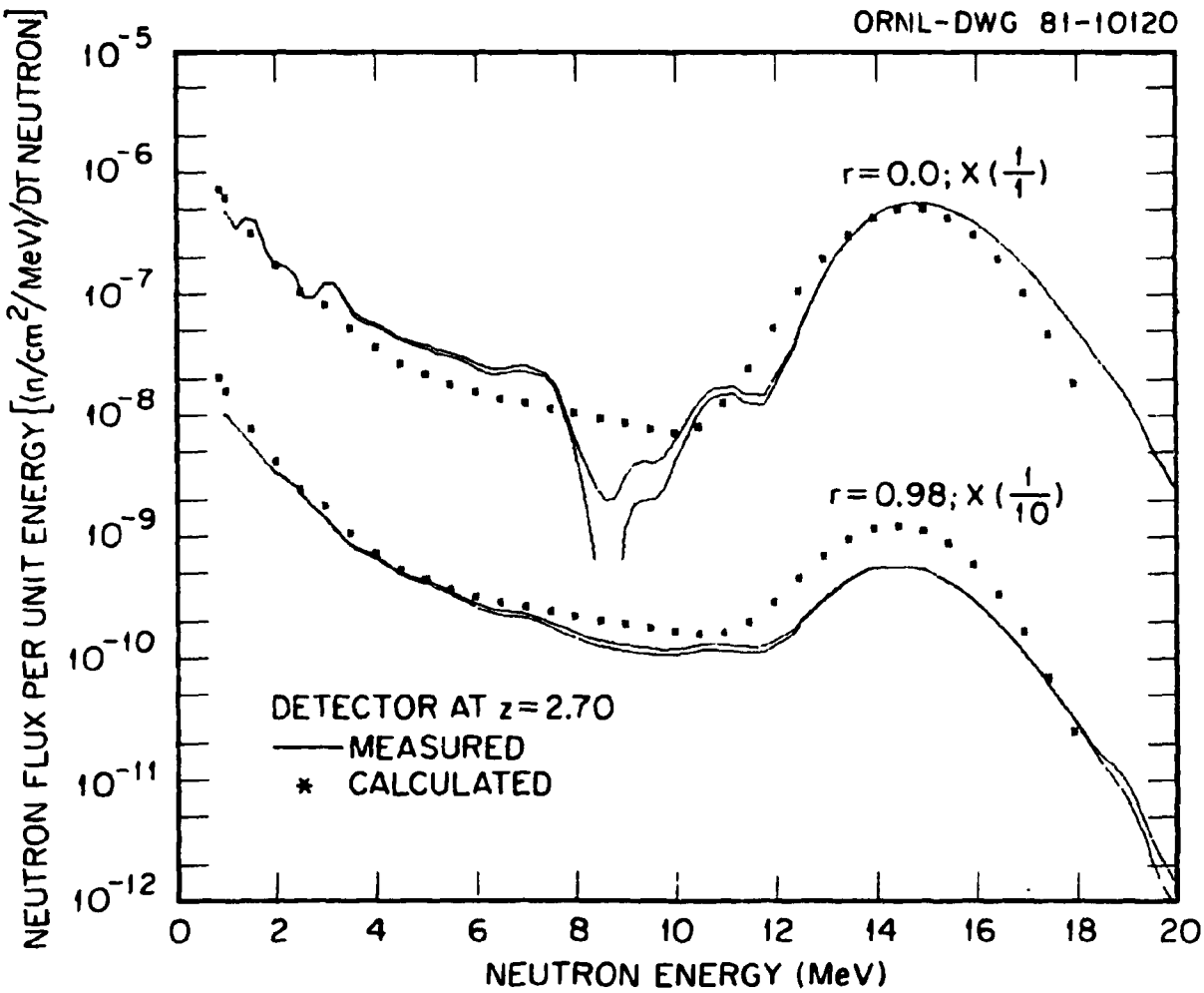


Fig. 8. Neutron flux per unit energy versus neutron energy for the detectors at z = 2.70 m; r = 0.0 and 0.98 m. The calculated data were obtained using discrete ordinates radiation transport methods.

distributions. The calculated data have been smoothed by convoluting the neutron flux per unit energy in each multigroup energy interval with an energy-dependent Gaussian response function having a width given by Eq. (2). The calculated and measured spectra are absolutely normalized to a source strength of one D-T neutron. For the purposes of displaying the data, some of the spectra have been multiplied by factors of $10^{-n}$, n = 1, 2, 3, etc. The actual magnitude of these spectra are restored by multiplying by the appropriate factor of $10^{n}$.

Inspection of Figs. 4-8 reveals that the calculated and measured spectra are generally in good agreement in the neutron energy range between 850 keV and ∿10 MeV. The neutrons that contribute to the spectra in this energy range result from inelastic reactions of the source and secondary neutrons in experimental apparatus or are those which have undergone multiple collisions in transit from the source to the detector. The angular distributions of these neutrons are, for the most part, nearly isotropic and are well represented in the discrete ordinates calculations by a $P_3$ Legendre polynomial expansion.

At neutron energies above ∿10 MeV, the agreement among the calculated and measured differential neutron energy spectra is less favorable and the agreement varies significantly as a function of detector location. The neutrons that contribute to the spectra in this energy range are either uncollided neutrons emanating directly from the source (particularly for the on-axis detectors) or are those that reach the detector as the result of a single scattering from the experimental apparatus, particularly the iron duct. These single scattered neutrons arise from both elastic and inelastic reactions which at energies above ∿10 MeV have angular

distributions that are very forward peaked. When the angular distribution is represented by a $P_3$ Legendre expansion, the angular dependence of the scattering probabilities are not adequately described. As a result, the neutron flux at the detector may be either over- or underestimated depending upon the angle at which the neutron scatters in transit from the source to the detector. This phenomena is most evident in the calculated spectra at the off-axis detector locations shown in Figs. 4-8.

When the detector is on the axis of the iron duct, r = 0.0, the neutron energy spectra above ~10 MeV is dominated by the uncollided neutrons emanating from the source and the impact on the spectra from neutrons that singly scatter to the detector is obscured. As the detector is displaced from the axis, r > 0.0, the influence on the neutron flux from the poorly represented angular distributions for neutron scattering become more obvious and dependent on detector location. The calculated neutron spectra over- and underestimate the energetic neutron response. Exceptions are noted when the detector is at z = 1.51 m, r = 0.19 m (Fig. 4) and at z = 2.08 m, r = 1.19 m (Fig. 6). In the former case, the detector is just in the shadow of the iron duct so the attenuation of the source neutrons is small since the neutrons traverse only a small distance in the iron and the high energy (>10 MeV) neutron flux is still dominated by the uncollided neutron flux. In the latter case, the detector is shielded from the iron duct by the concrete support shield and the probability for a neutron reaching the detector as the result of a single scattering from the duct is considerably reduced.

In order to assess the impact of single scattering on the neutron energy spectra, the discrete ordinates calculations were carried out using a $P_7$ Legendre polynomial expansion to represent the neutron scattering cross sections. Although some improvement was noted in the agreement between the calculated and measured spectra, it became apparent that satisfactory comparisons required an even higher order of expansion to account for the single scattered neutron contribution to the high energy neutron flux. As a result, the following calculational procedure was adopted.

In the discrete ordinates (DO) calculations, the total neutron scalar flux in energy group g at detector location $\vec{r}_d$ is

$$\phi_{r,g}(\vec{r}_d,DO,P_3) = \phi_{u,g}(\vec{r}_d) + \phi_{c,g}(\vec{r}_d,DO,P_3) \qquad (6)$$

where

$\phi_{u,g}(\vec{r}_d)$ = the uncollided neutron scalar flux in energy group g at detector location $\vec{r}_d$ and

$\phi_{u,g}(\vec{r}_d,DO,P_3)$ = the collided neutron scalar flux in energy group g at detector location $\vec{r}_d$.

The notation, $P_3$, means that the collided neutron scalar flux is calculated using a $P_3$ Legendre polynomial expansion of the neutron scattering cross sections.

The uncollided neutron scalar flux is calculated in the GRTUNCL code which solves the equations of the form

$$\phi_{u,g} = \frac{S_g(\vec{r}_t)\exp[-\beta_g(\vec{r}_t,\vec{r}_d)]}{4\pi|\vec{r}_d-\vec{r}_t|^2} \qquad (7)$$

where

$S_g(\vec{r}_t)$ = the neutron source in energy group g at the target, $\vec{r}_t$, and

$\beta_g(\vec{r}_t,\vec{r}_d)$ = the number of mean free paths along the vector from the target location $\vec{r}_t$ to the detector location $\vec{r}_d$.

The uncollided neutron scalar flux is not calculated using the discrete ordinates method or the $P_3$ scattering cross sections. The uncollided flux can be obtained analytically. GRTUNCL does, however, also calculate the spatially dependent first collision neutron source, $S_g^1(\vec{r},P_3)$, using the $P_3$ cross section data. The single scattered and multiply collided neutron scalar flux contributions to the total neutron scalar flux are calculated in the DOT-FALSTF sequence and combine to form the collided neutron scalar flux, $\phi_{c,g}(\vec{r}_d,DO,P_3)$. That is,

$$\phi_{c,g}(\vec{r}_d,DO,P_3) = \phi_{SS,g}(\vec{r}_d,DO,P_3) + \phi_{MC}(\vec{r}_d,DO,P_3) \qquad (8)$$

where

$\phi_{SS,g}(\vec{r}_d,DO,P_3)$ = the single scattered neutron scalar flux in energy group g at detector location $\vec{r}_d$ and

$\phi_{MC,g}(\vec{r}_d,DO,P_3)$ = the mutiply collided neutron scalar flux in energy group g at detector location $\vec{r}_d$

A version of the Monte Carlo code MORSE[20] was recently developed that carries out the transport of neutrons by sampling from cross section data that are continuous in energy rather than averaged over multigroup energy intervals. Another important feature of this code, called PXMORSE, is that neutron scattering angles are obtained by sampling directly from the angular distributions that are represented using the Legendre coefficients given in the ENDF/B-IV data files. For example, the angular distributions for 14-MeV neutron elastic scattering in iron are estimated by sampling from an angular distribution that is approximated using a $P_{12}$ Legendre expansion. The sequence of calculations that were carried out using the PXMORSE code are shown on the right-hand side of Fig. 3. The two-dimensional geometry of the experiment, shown in Fig. 2, was modeled for use in the Monte Carlo calculations using the Combinatorial Geometry Package described in Ref. 20. The neutron source was obtained by sampling from probability density functions constructed from the energy-angle distributions for neutrons produced in D-T reactions given in Table II. Neutrons that reached the detectors with energies above 10 MeV as the result of a single elastic or inelastic scattering were calculated using next-flight estimation techniques. The single scattered neutron flux at each detector location was binned in energy groups having the same boundaries as the multigroup energy data used in the discrete ordinates calculations. Thus, the PXMORSE calculational sequence (MC) yields the single scattered neutron scalar flux in energy group g at detector location $\vec{r}_d$ with the angular distributions for neutron scattering represented by a Legendre polynomial of order $\ell$, where $\ell$ is defined by the coefficients in the ENDF/B-IV data files for neutron scattering at

energy $E_n$; that is, $\phi_{SS,g}(\vec{r}_d,MC,P_\ell)$.

As noted above, the GRTUNCL code calculates the spatially dependent first collision neutron source distribution in the geometry of the experiment. If these data are used as the input to the FALSTF code, as indicated on the left-hand side of Fig. 3, the single scattered neutron flux term, $\phi_{SS,g}(\vec{r}_d,DO,P_3)$, generated in the GRTUNCL-DOT-FALSTF sequence is reproduced. That is, FALSTF solves an equation of the form

$$\phi_{SS,g}(\vec{r}_d,DO,P_3) = \frac{S^1_g(\vec{r}_d,P_3)\exp[-\beta_g(\vec{r},\vec{r}_d)]}{4\pi|\vec{r}_d-\vec{r}|^2} \qquad (9)$$

where $\beta_g(\vec{r},\vec{r}_d)$ is the number of mean free paths along the vector from the source location $\vec{r}$ to the detector $\vec{r}_d$.

Since the single scattered neutron flux impacts the calculated spectra predominately above 10 MeV, the corrections to the scattering were made only at 10 MeV and above. Now, the total neutron scalar flux at each detector can be obtained by subtracting the single scattered neutron scalar flux calculated using Eq. (9) from the total neutron scalar flux given by Eq. (6) and then adding the single scattered neutron flux obtained from PXMORSE. Then,

$$\phi_{T,g}(\vec{r}_d;DO,P_3;MC,P_\ell) = \phi_{u,g}(\vec{r}_d) + \phi_{MC}(\vec{r}_d,DO,P_3) + \phi_{SS}(\vec{r}_d,MC,P_\ell) \qquad (10)$$

The gamma ray energy spectra were calculated using only the discrete ordinates segment of the radiation transport calculational sequence. Gamma radiation is emitted nearly isotropically and can, therefore, be well approximated using a $P_3$ Legendre expansion of the cross section data.

## IV. DISCUSSION OF RESULTS

The differential neutron energy spectra calculated using the complete radiation transport code sequence shown in Fig. 2 are compared with the measured spectra in Figs. 9-13. The data are compared for neutrons with energies above 850 keV and are absolutely normalized to one D-T source neutron. As noted previously, the solid curves show the measured spectra and the points are the calculated data. In these comparisons, two sets of calculated data are given for each detector location at neutron energies above ∿10 MeV. These points indicate the upper and lower bounds on the calculated spectra due to the statistical variation in the estimated single scattered neutron scalar flux introduced by the Monte Carlo calculation. The band defined by these points represents plus or minus one standard deviation in the calculated data. The appearance in both the calculated and measured neutron energy spectra of flux above ∿15 MeV is introduced by the Gaussian response of the detector. It is not kinematically possible for 250 keV deuterons to produce neutrons with energies above 15.1 keV in the D-T reaction.

Comparison of these data with those shown in Figs. 4-8 reveal that considerable improvement has been achieved among the calculated and experimental spectra when the calculated data are obtained using the complete radiation transport sequence with the improved treatment of neutron single scattering.

Consider the cases where the detector is on the axis of the duct, ie., r = 0.0. The agreement between the calculated and measured neutron energy is favorable above ∿10 MeV. In the neutron energy range between ∿11 and ∿13 MeV, the calculated data are systematically higher than the

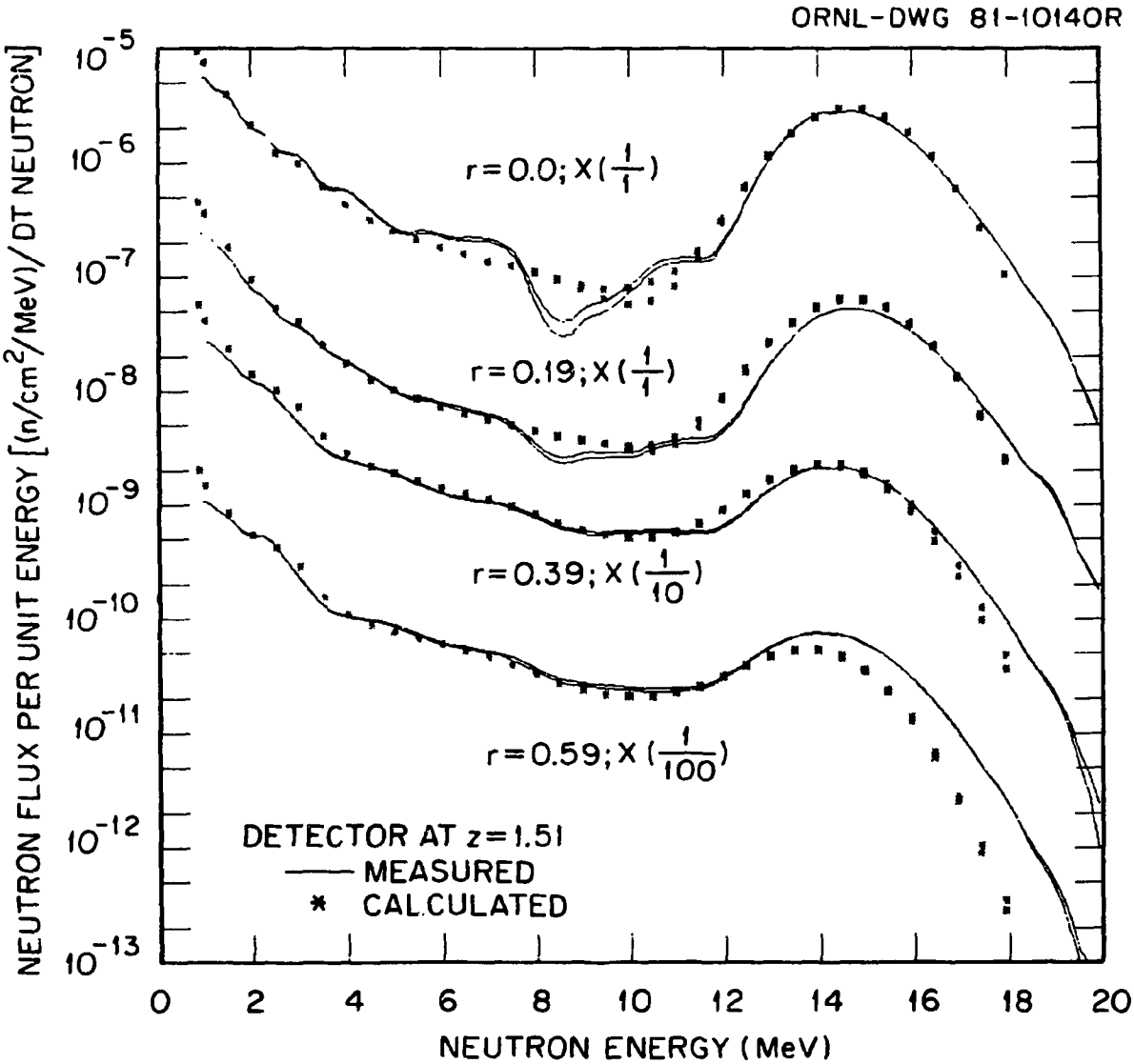


Fig. 9. Neutron flux per unit energy versus neutron energy for the detectors z = 1.51 m; r = 0.0, 0.19, 0.39, and 0.59 m. The calculated data were obtained using both discrete ordinates and Monte Carlo radiation transport methods.

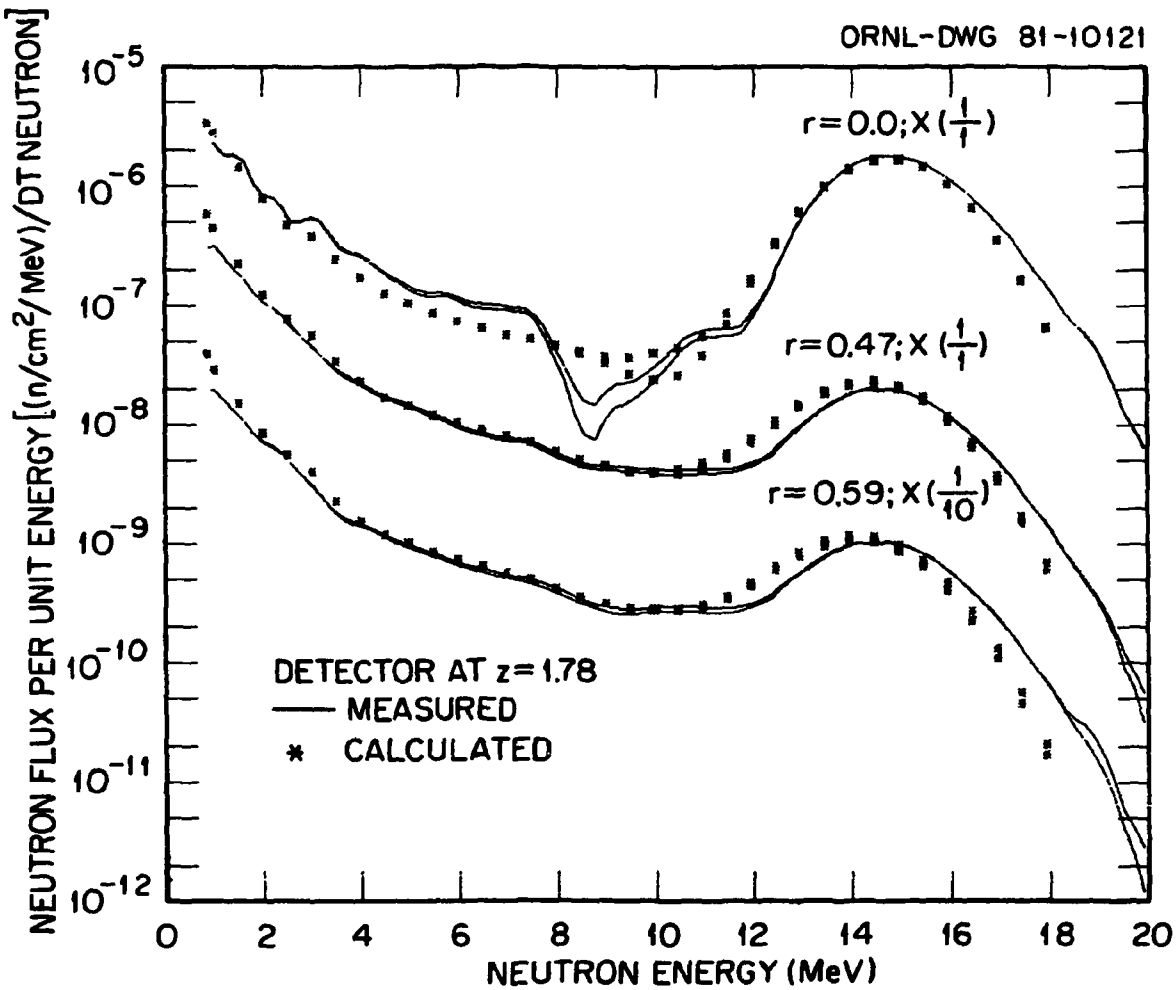


Fig. 10. Neutron flux per unit energy versus neutron energy for the detectors at z = 1.78 m; r = 0.0, 0.47, and 0.59 m. The calculated data were obtained using both discrete ordinates and Monte Carlo radiation transport methods.

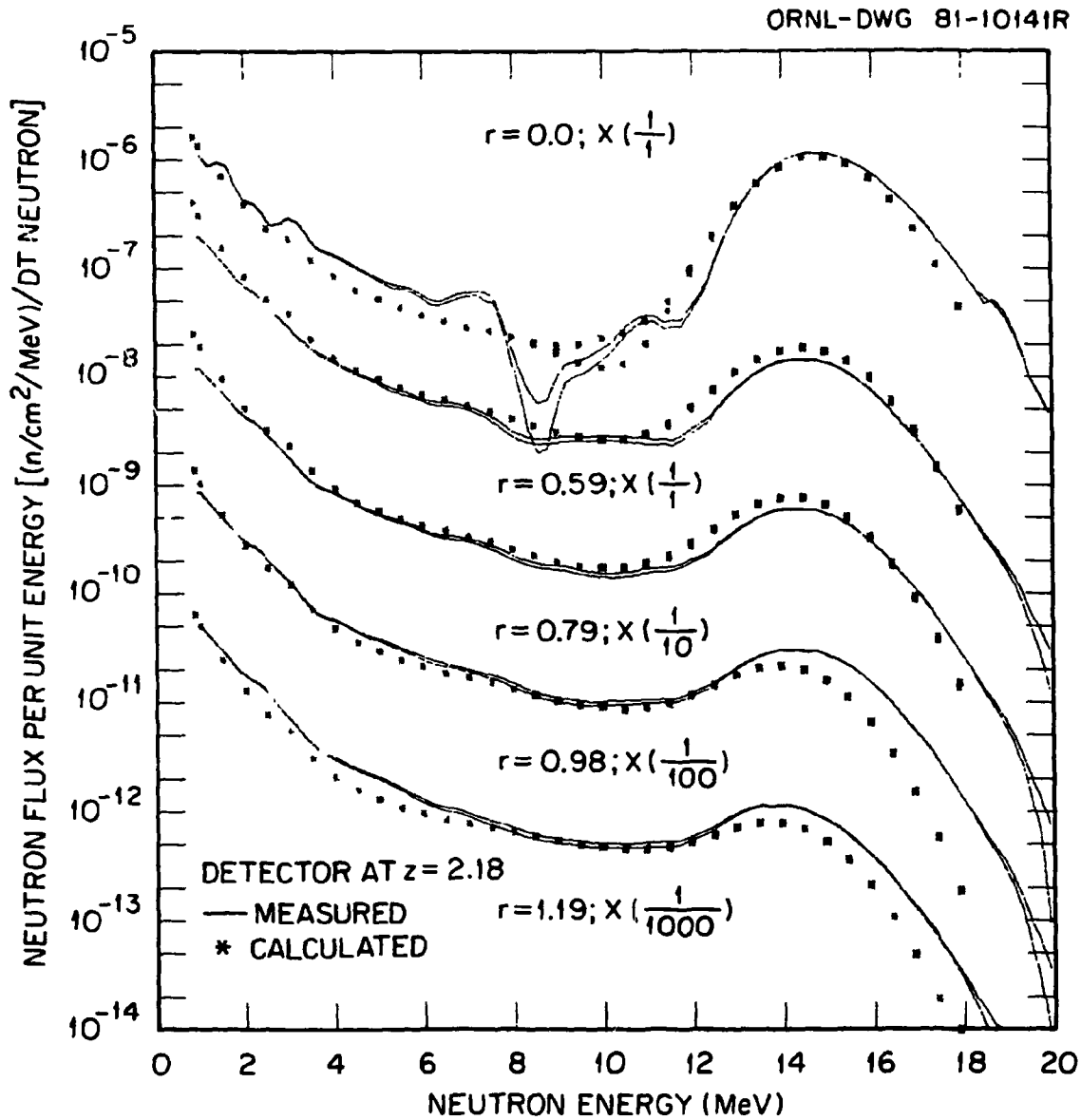


Fig. 11. Neutron flux per unit energy versus neutron energy for the detectors at z = 2.08 m; r = 0.0, 0.59, 0.79, 0.98, and 1.19 m. The calculated data were obtained using both discrete ordinates and Monte Carlo radiation transport methods.

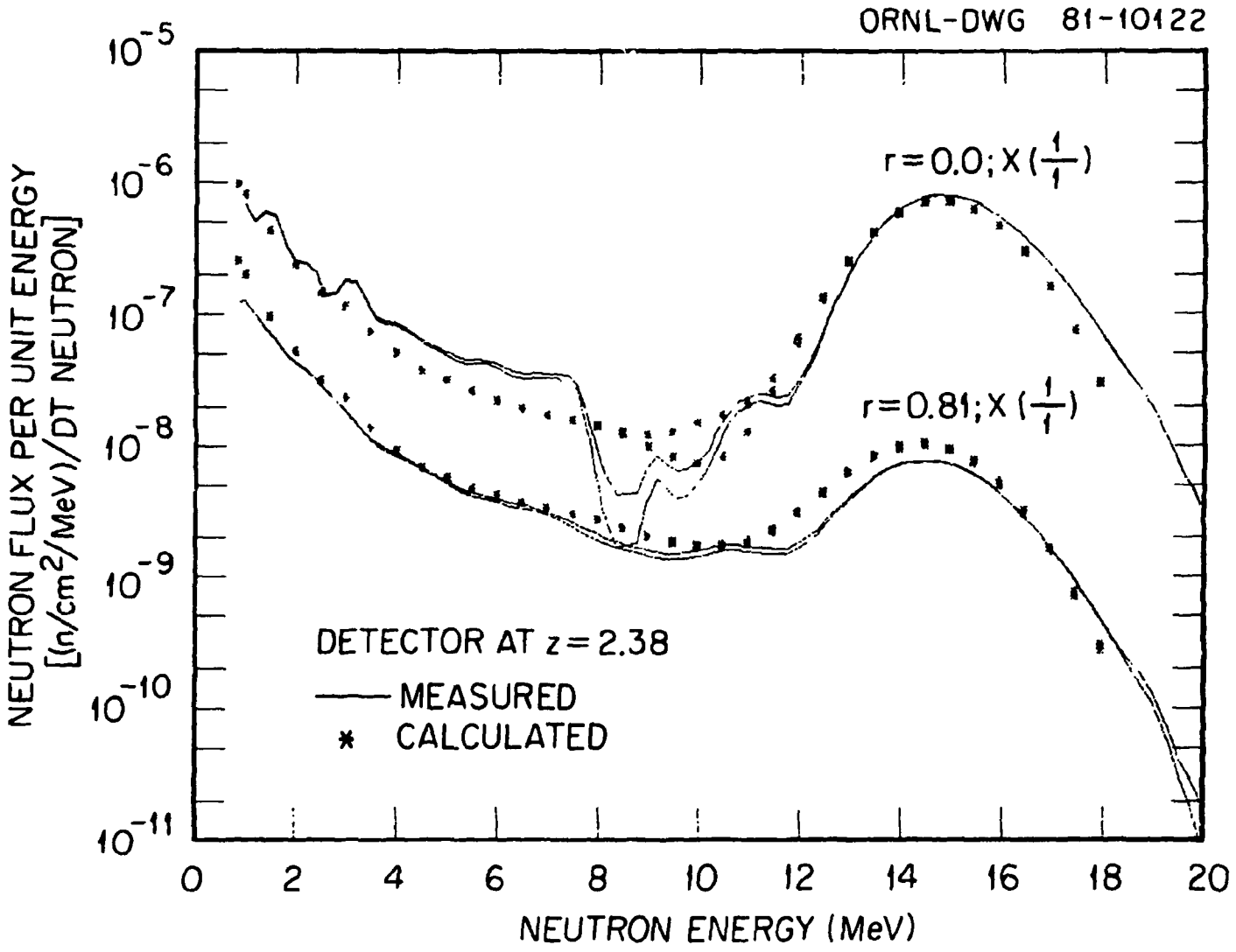


Fig. 12. Neutron flux per unit energy versus neutron energy for the detectors at z = 2.38 m; r = 0.0 and 0.81 m. The calculated data were obtained using both discrete ordinates and Monte Carlo radiation transport methods.

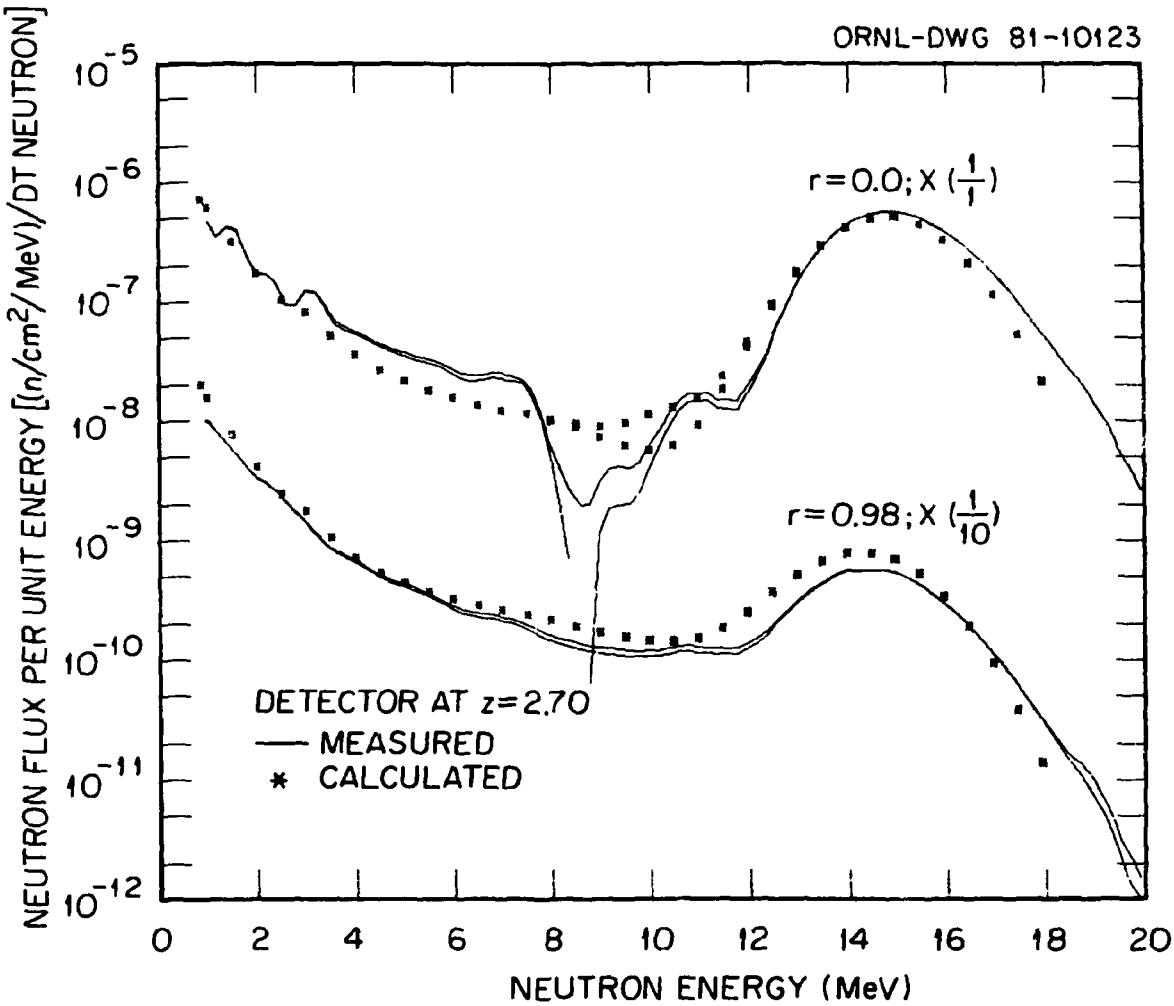


Fig. 13. Neutron flux per unit energy versus neutron energy for the detectors at z = 2.70 m; r = 0.0 and 0.98 m. The calculated data were obtained using both discrete ordinates and Monte Carlo radiation transport methods.

measured data, but the difference between the calculated and measured data is reduced by as much as 30% compared to the same spectra shown in Figs. 4-8. The calculated data are higher than the measured data between 8 and 11 MeV while the converse is true at neutron energies between 850 keV and 8 MeV. The dip in the measured spectra between 8 and 11 MeV results from the unfolding of the measured pulse height spectra. When the detector is on the axis of the duct, the uncollided neutrons dominate the spectrum and the uncollided-to-collided neutron flux ratio above 8 MeV is large. The optimum unfolding of the pulse-height spectrum for the detector on-axis should yield a high energy neutron peak that is separated from the low-energy tail. The resolution of the detector and the differential nonlinearity introduced by the electronics, "smear" the pulse-height data and the FERD[10] unfolding code has difficulty in separating the high and low energy components in the spectrum.

For the cases were the detector is off the axis of the duct, $r > 0.0$, the agreement between the calculated and measured neutron energy spectra has been considerably improved compared to the results shown in Figs. 4-8. The calculated and measured spectra are in good agrement between 850 keV and 10 MeV at all detector locations. At neutron energies above 10 MeV, the calculated spectra are in good agreement with the measured data at nearly all detector locations. The calculated spectra for the detectors at $z = 1.51$ m, $r = 0.59$ m (Fig. 9) and $z = 2.08$ m, $r = 0.98$ m (Fig. 11) more nearly reproduce the measured spectra compared to the previous results shown in Figs. 4 and 6, respectively. For the detector locations $z = 2.38$ m, $r = 0.81$ m and $z = 2.70$ m, $r = 0.98$ m the calculated spectra are still higher than the measured data at energies above 10 MeV, but

the magnitude of the calculated neutron flux per unit energy has been reduced by nearly a factor of two compared to the data shown in Figs. and 8.

The nuclear performance of fusion reactor components is most often assessed in terms of integrated neutron responses. From this point of view, therefore, it is more relevant to compare the calculated and measured energy integrated neutron spectra. These data are shown in Figs. 14-18 and were obtained by integrating the differential neutron spectra shown in Figs. 9-13. For the cases were the detector is on the axis, r = 0.0, the calculated and measured data agree within $\lesssim$10% over the neutron energy range from 850 keV to $\sim$15 MeV. At energies above 15 MeV, the calculated spectra are lower than the measured data, but the difference is due mainly to the Gaussian smoothing of spectra. At the off-axis detector locations, the agreement among the measured and calculated spectra varies by as much as ±50% depending on the detector location.

The calculated differential and integral gamma ray spectra are compared with the measured spectra in Figs. 19-28. These spectra are compared for gamma rays having energies above 750 keV. The calculated data were obtained by convoluting the gamma ray flux per unit energy in each multigroup energy interval with an energy dependent Gaussian response function having a width given by Eq. (3). All of the calculated data were obtained using the discrete ordinates segment of the radiation transport code network in Fig. 3. Gamma rays produced from inelastic and neutron capture reactions have nearly isotropic angular distributions and are well represented in the discrete ordinates transport calculations by a $P_3$ Legendre

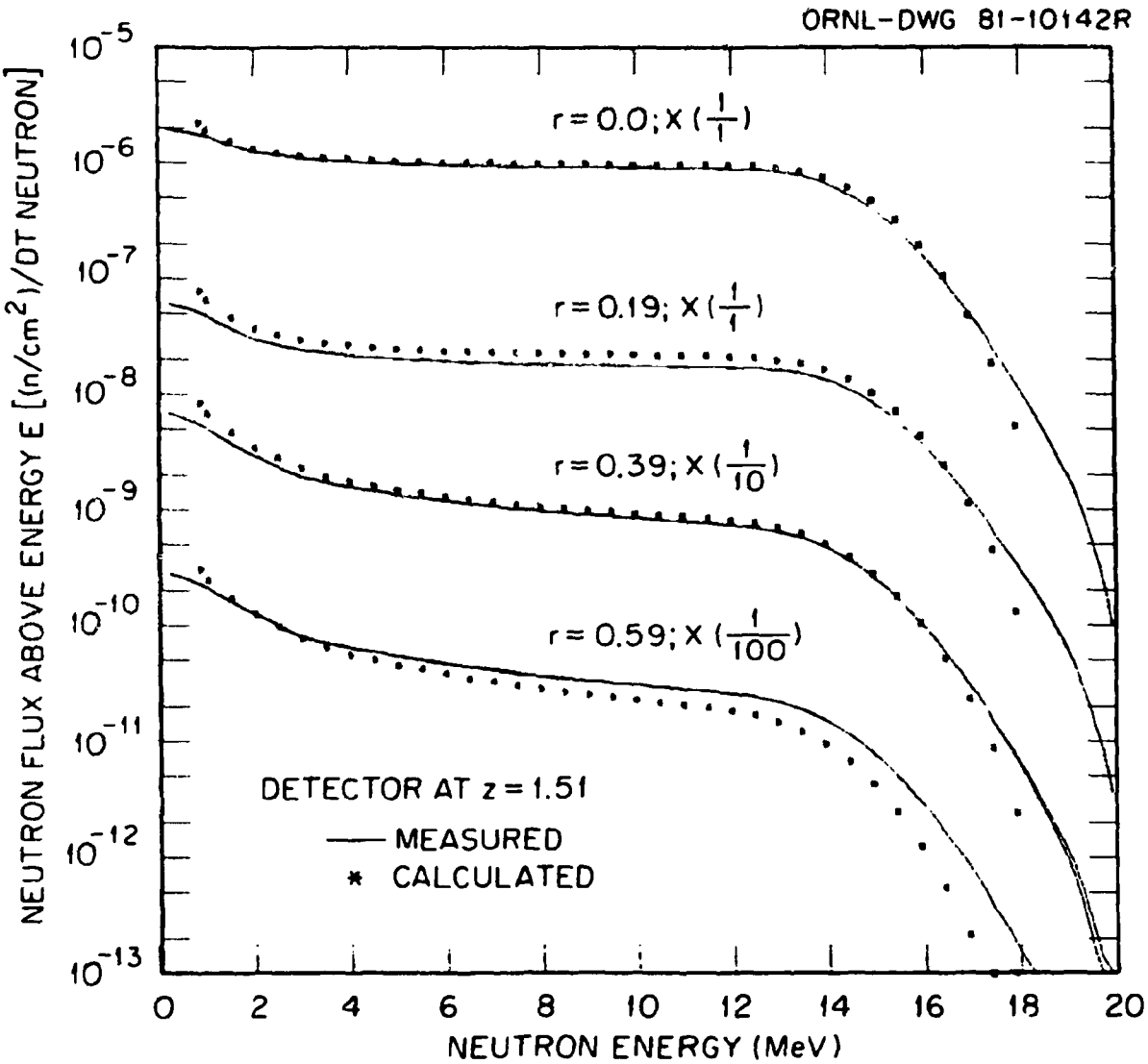


Fig. 14. Neutron flux above energy E versus neutron energy for the detectors at z = 1.51 m; r = 0.0, 0.19, 0.39, and 0.59 m. The calculated data were obtained using both discrete ordinates and Monte Carlo radiation transport methods.

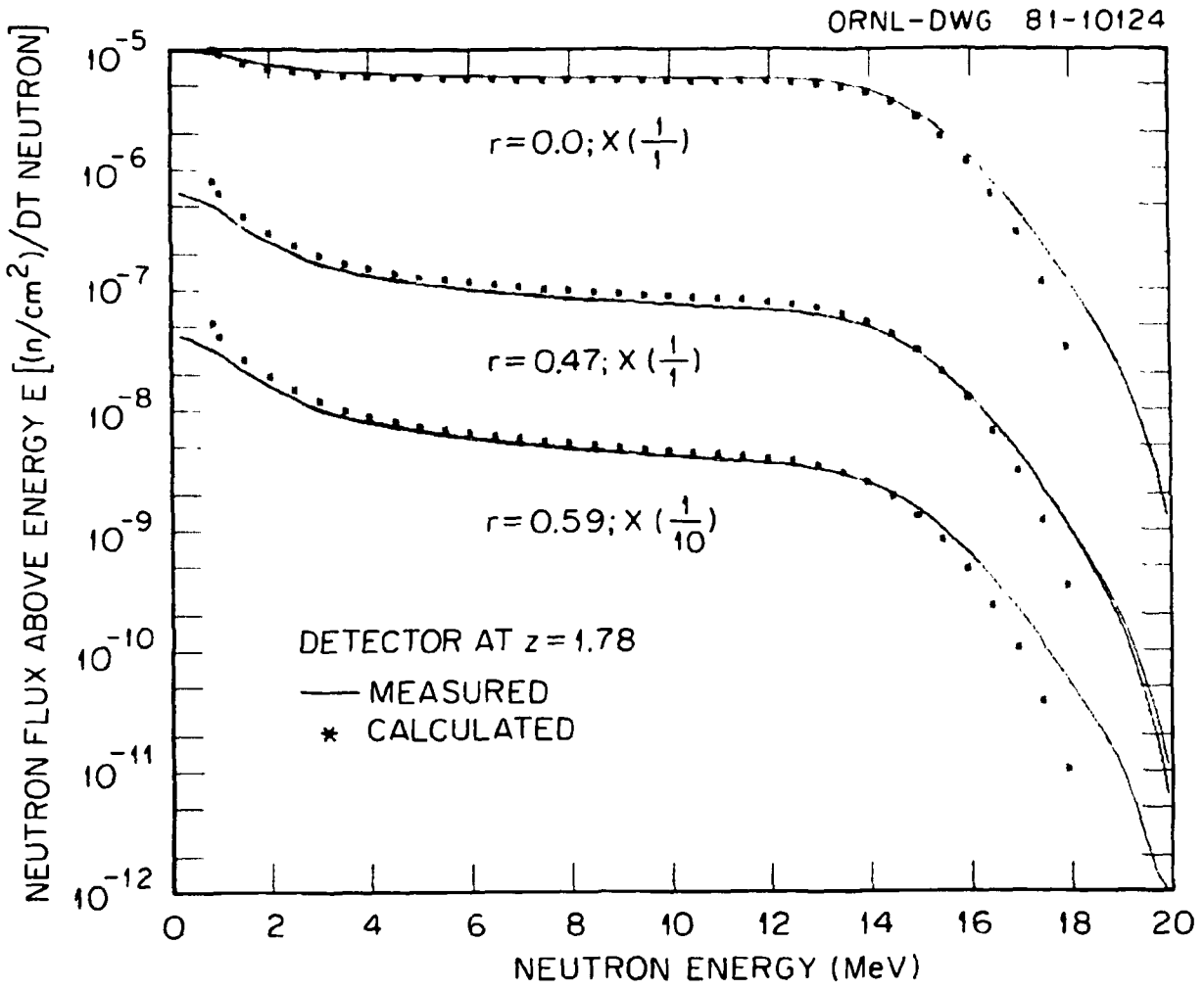


Fig. 15. Neutron flux above energy E versus neutron energy for the detectors at z = 1.78 m; r = 0.0, 0.47, and 0.59 m. The calculated data were obtained using both discrete ordinates and Monte Carlo radiation transport methods.

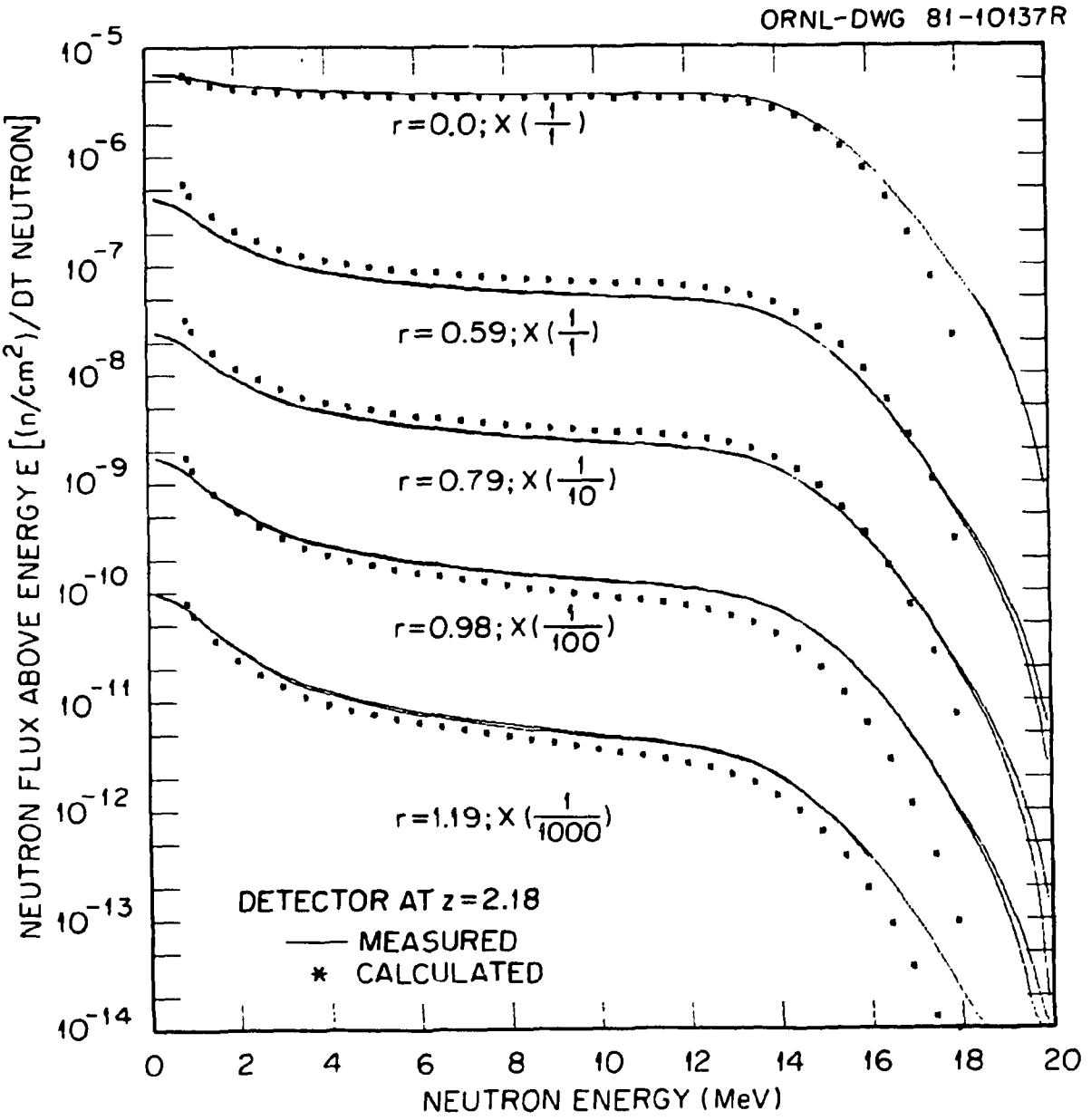


Fig. 16. Neutron flux above energy E versus neutron energy for the detectors at z = 2.08 m; r = 0.0, 0.59, 0.79, 0.98, and 1.19 m. The calculated data were obtained using both discrete ordinates and Monte Carlo radiation transport methods.

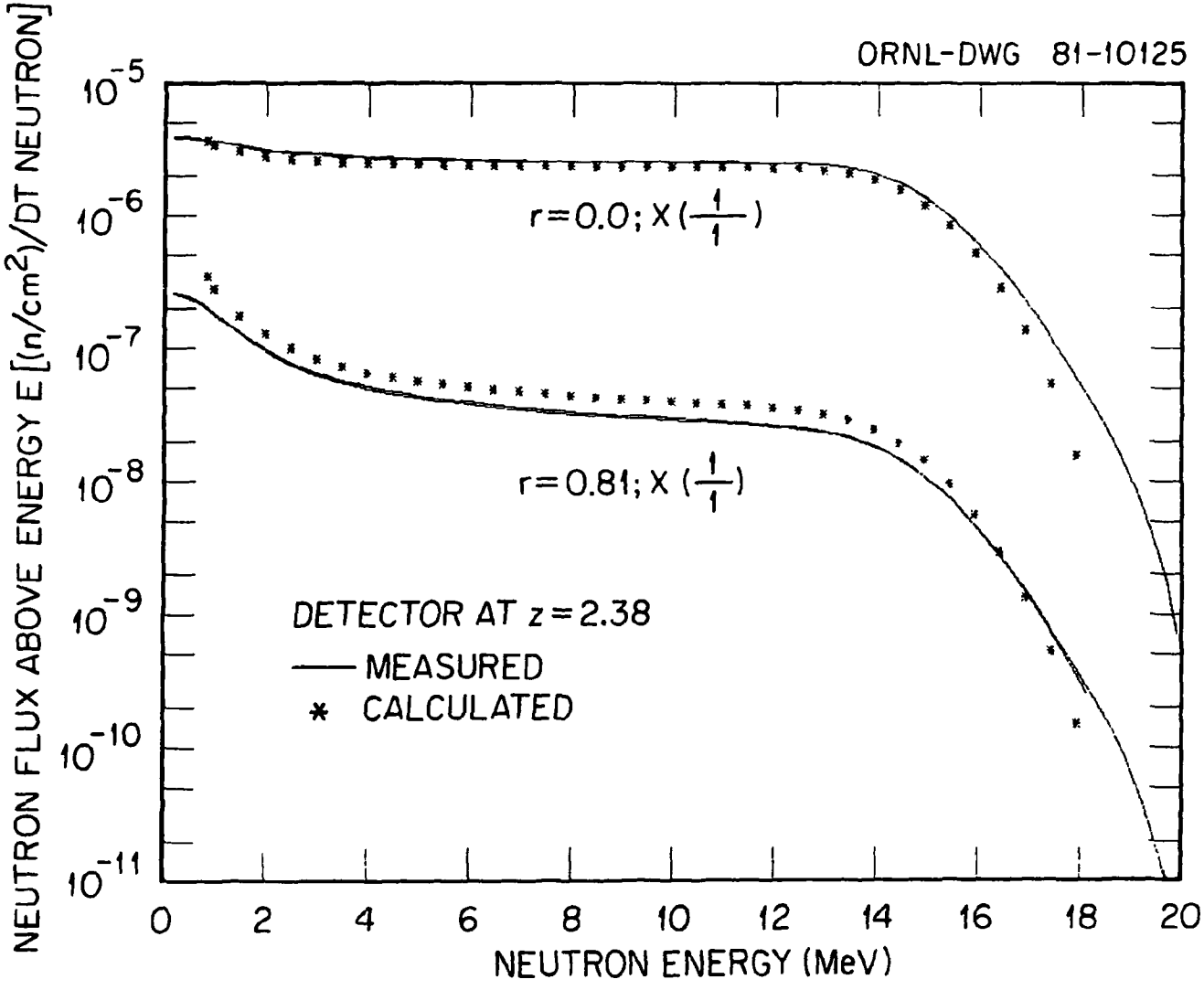


Fig. 17. Neutron flux above energy E versus neutron energy for the detectors at z = 2.38 m; r = 0.0 and 0.81 m. The calculated data were obtained using both discrete ordinates and Monte Carlo radiation transport methods.

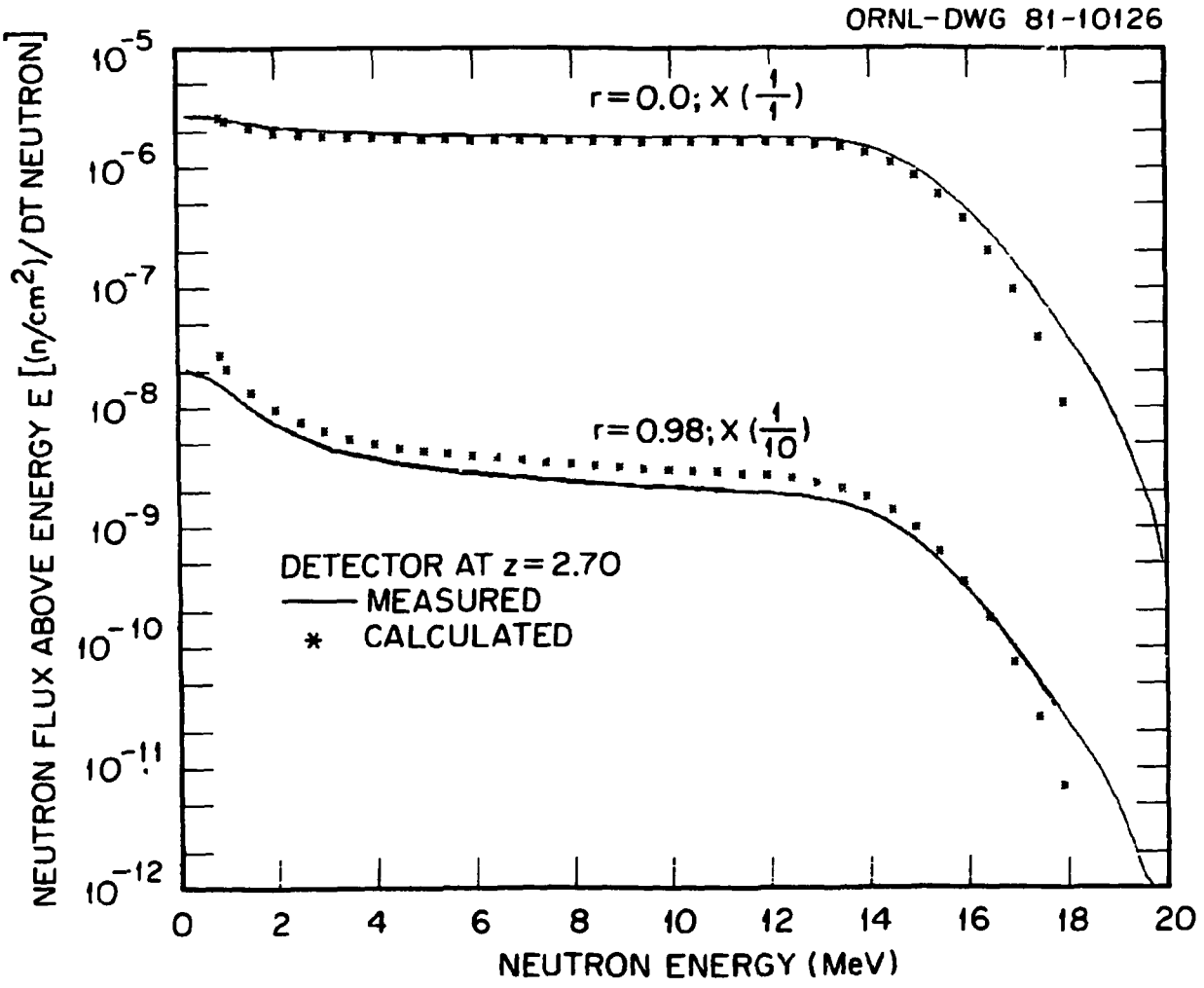


Fig. 18. Neutron flux above energy E versus neutron energy for the detectors at z = 2.70 m; r = 0.0 and 0.98 m. The calculated data were obtained using both discrete ordinates and Monte Carlo radiation transport methods.

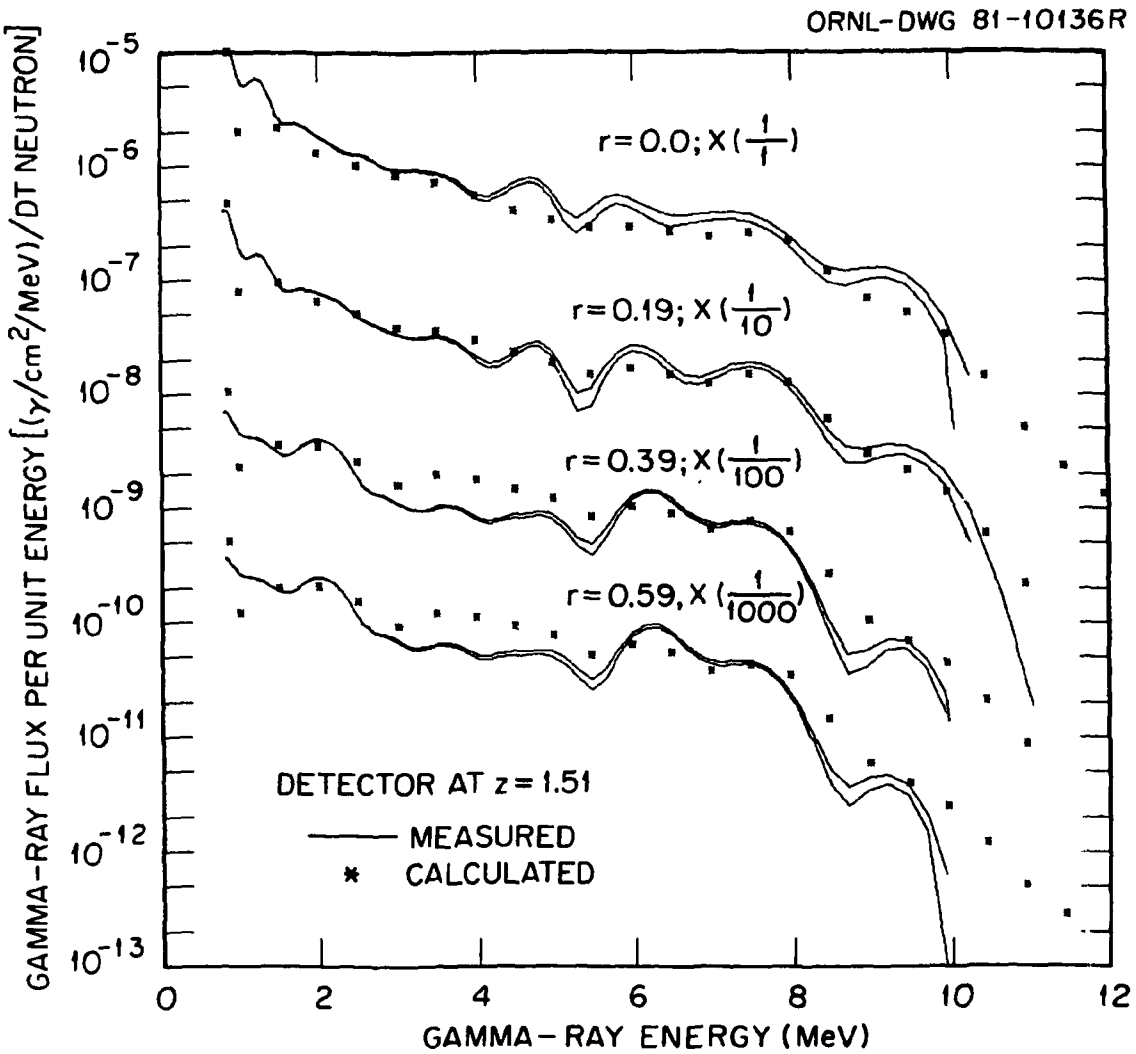


Fig. 19. Gamma ray flux per unit energy versus gamma ray energy for the detectors at z = 1.51 m; r = 0.0, 0.19, 0.39, and 0.59 m.

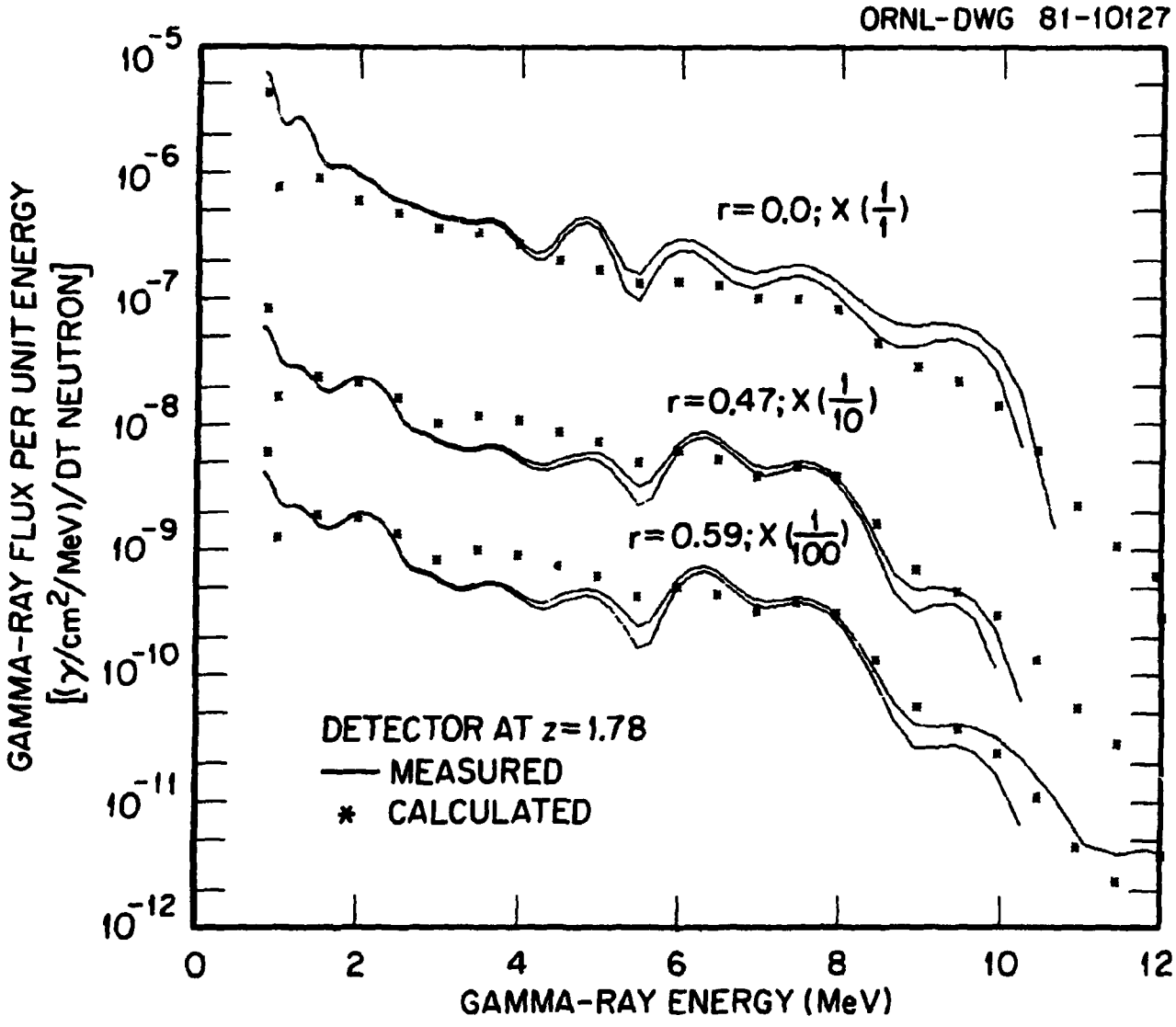


Fig. 20. Gamma ray flux per unit energy versus gamma ray energy for the detectors at z = 1.78 m; r = 0.0, 0.47, and 0.59 m.

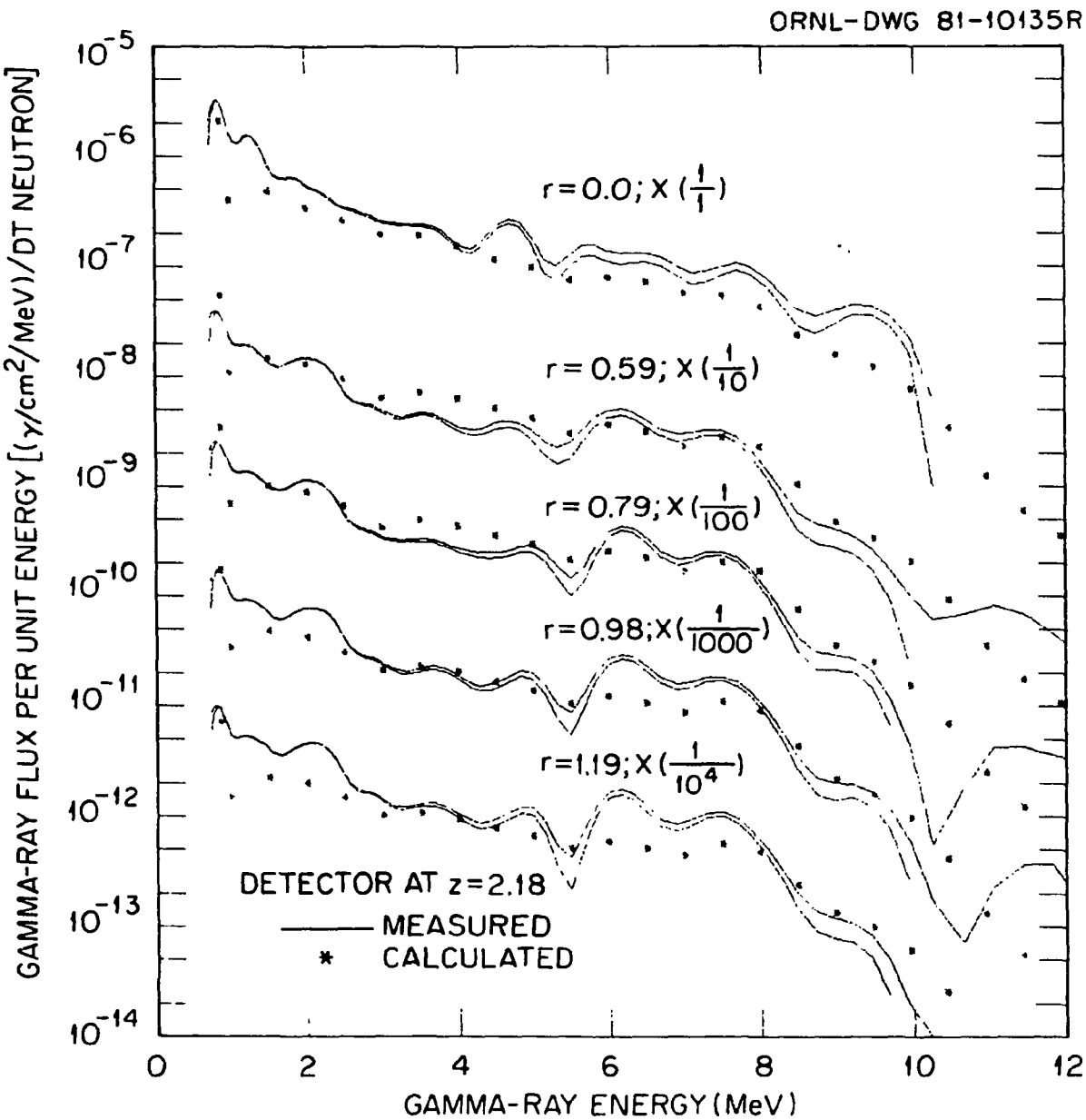


Fig. 21. Gamma ray flux per unit energy versus gamma ray energy for the detectors at z = 2.08 m; r = 0.0, 0.59, 0.79, 0.98, and 1.19 m.

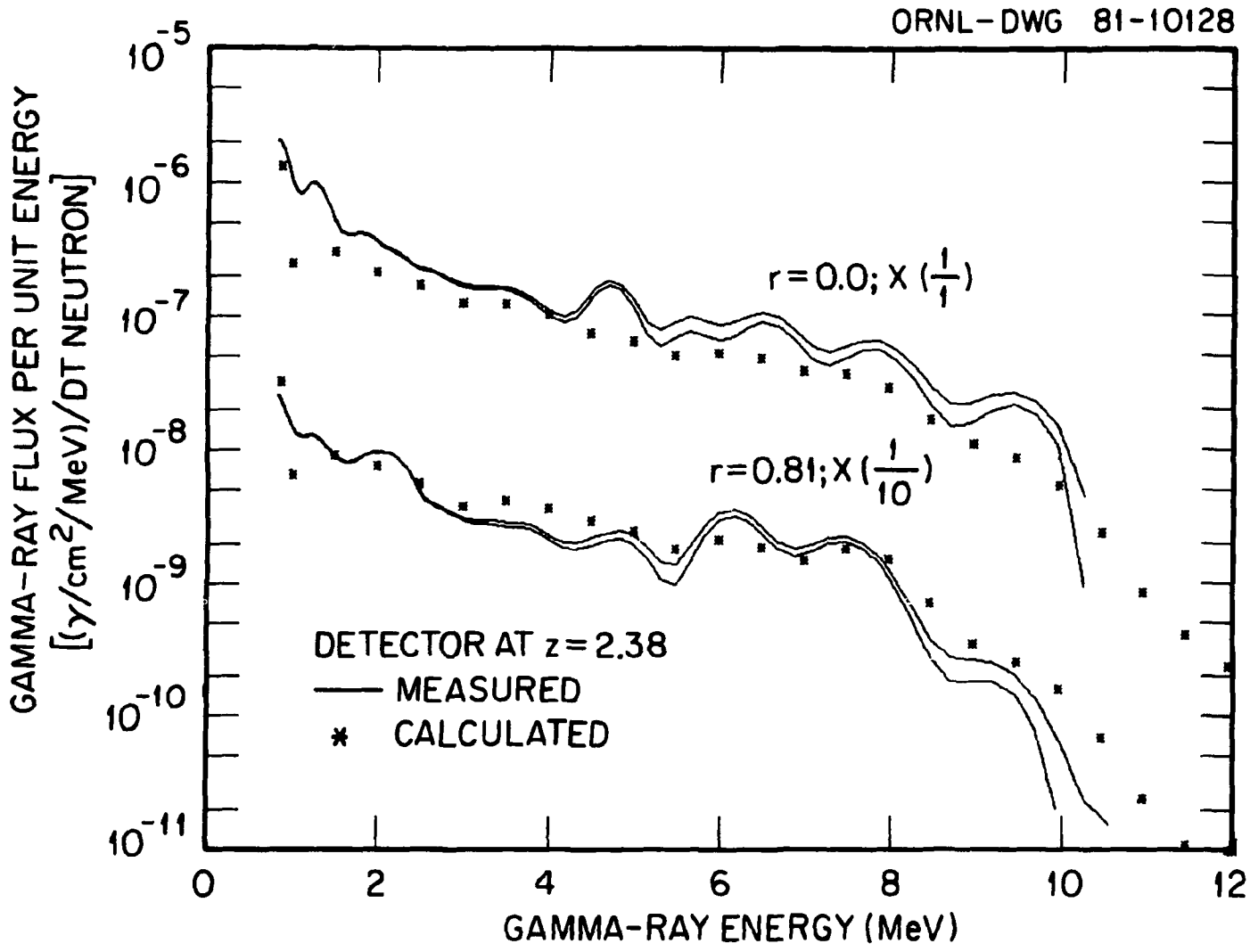


Fig. 22. Gamma ray flux per unit energy versus gamma ray energy for the detectors at z = 2.38 m; r = 0.0 and 0.81 m.

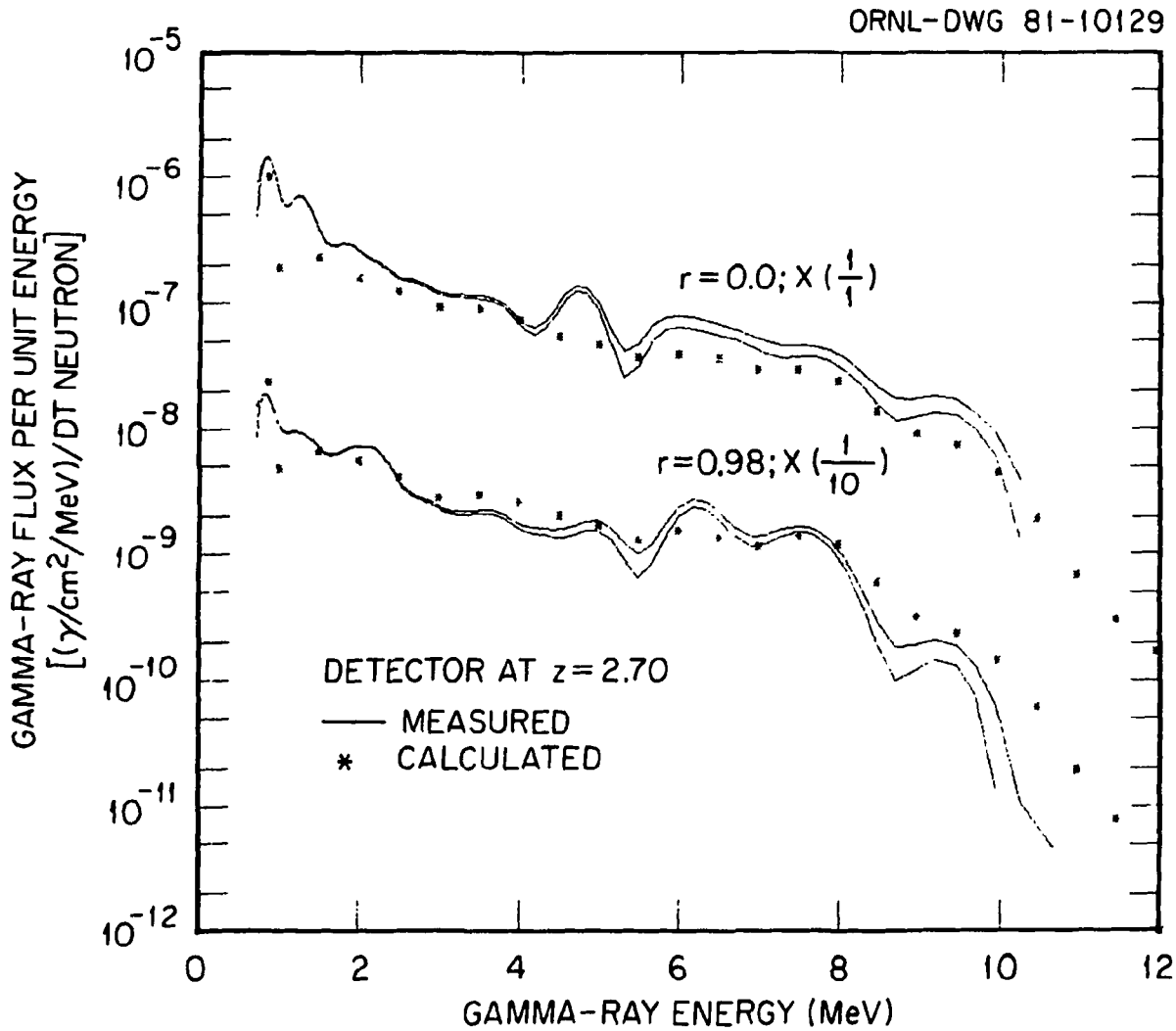


Fig. 23. Gamma ray flux per unit energy versus gamma ray energy for the detectors at z = 2.70 m; r = 0.0 and 0.98 m.

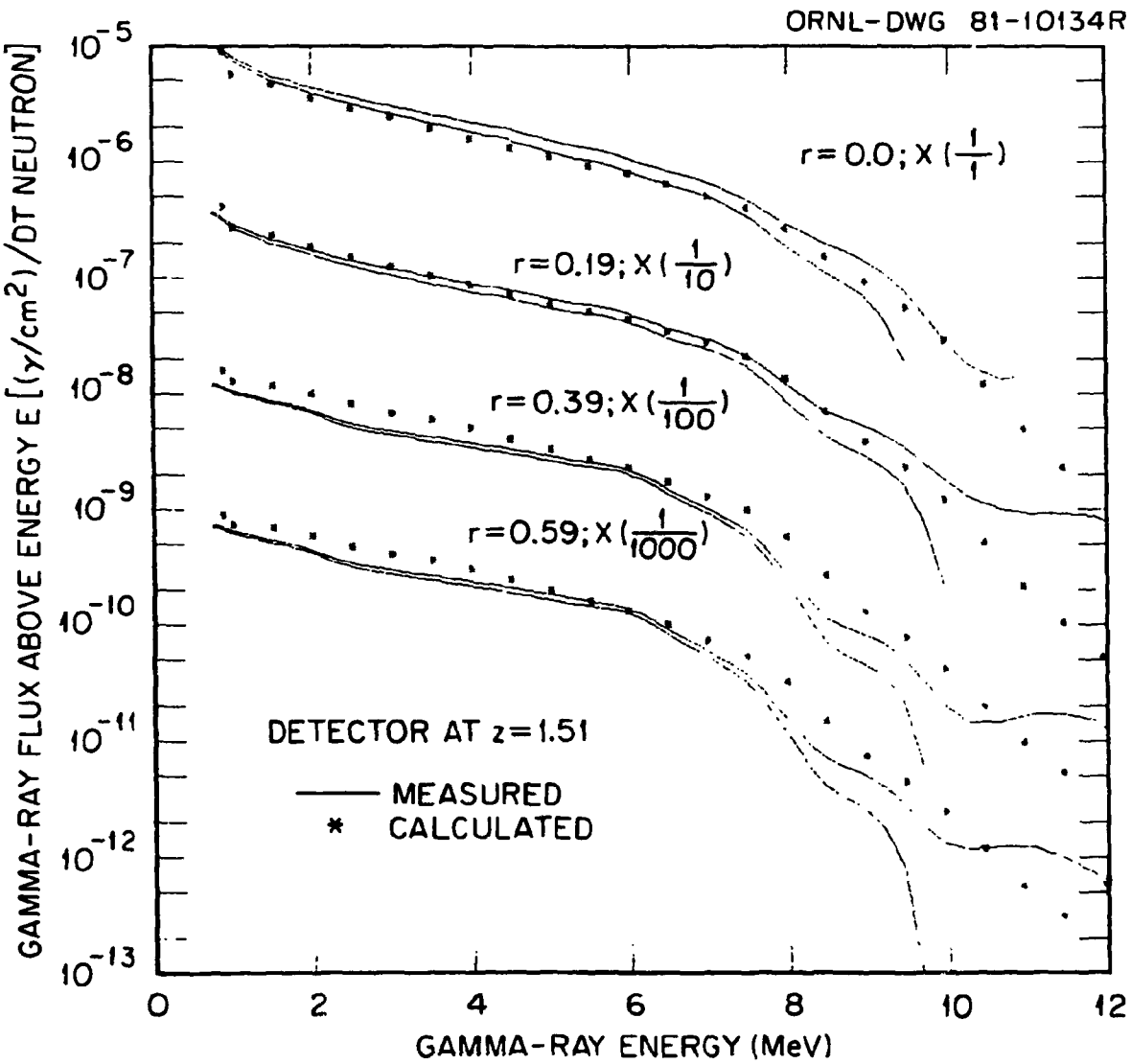


Fig. 24. Gamma ray flux above energy E versus gamma ray energy for the detectors at z = 1.51 m; r = 0.0, 0.19, 03.9, and 0.59 m.

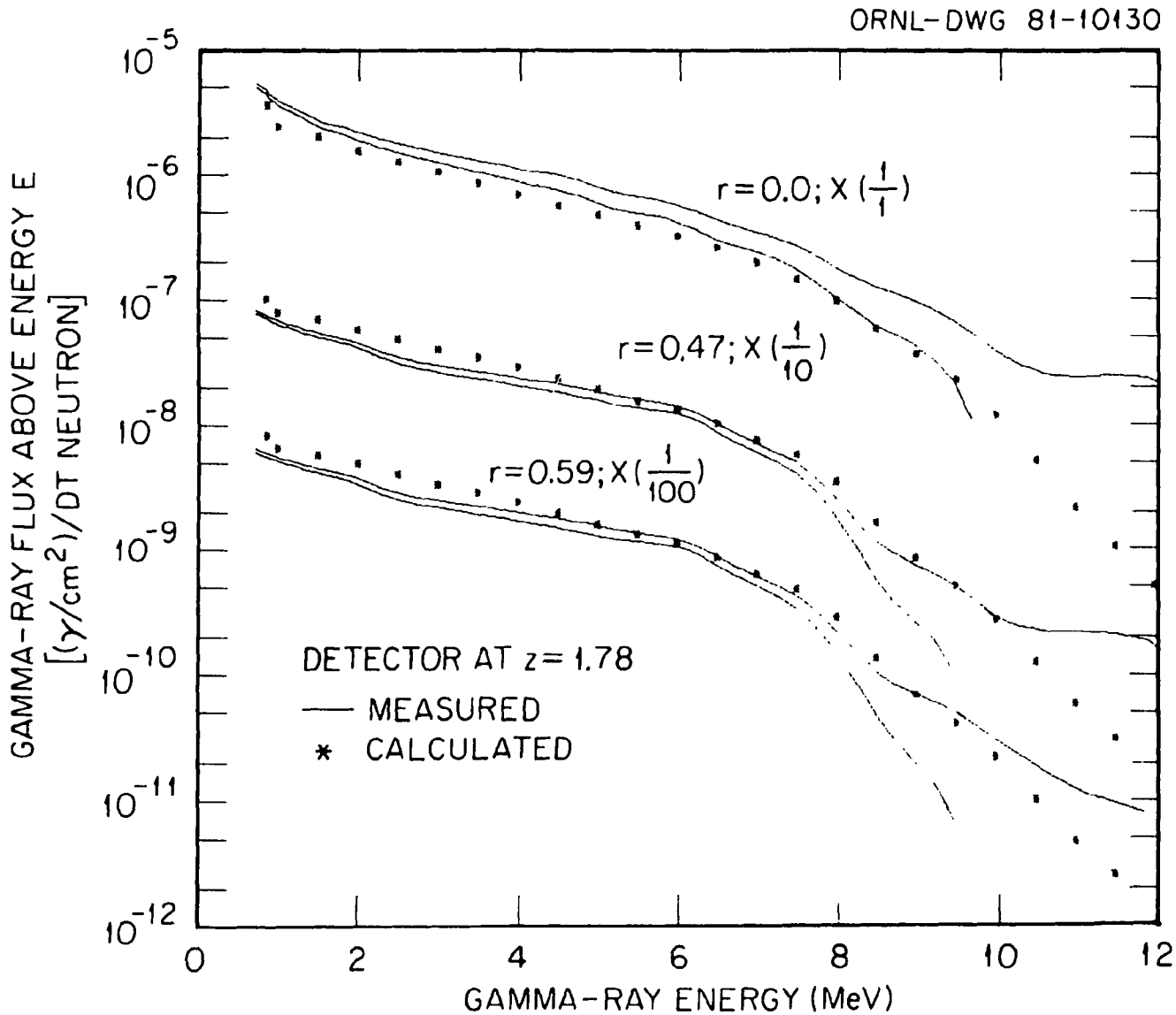


Fig. 25. Gamma ray flux above energy E versus gamma ray energy for the detectors at z = 1.78 m; r = 0.0, 0.47, and 0.59 m.

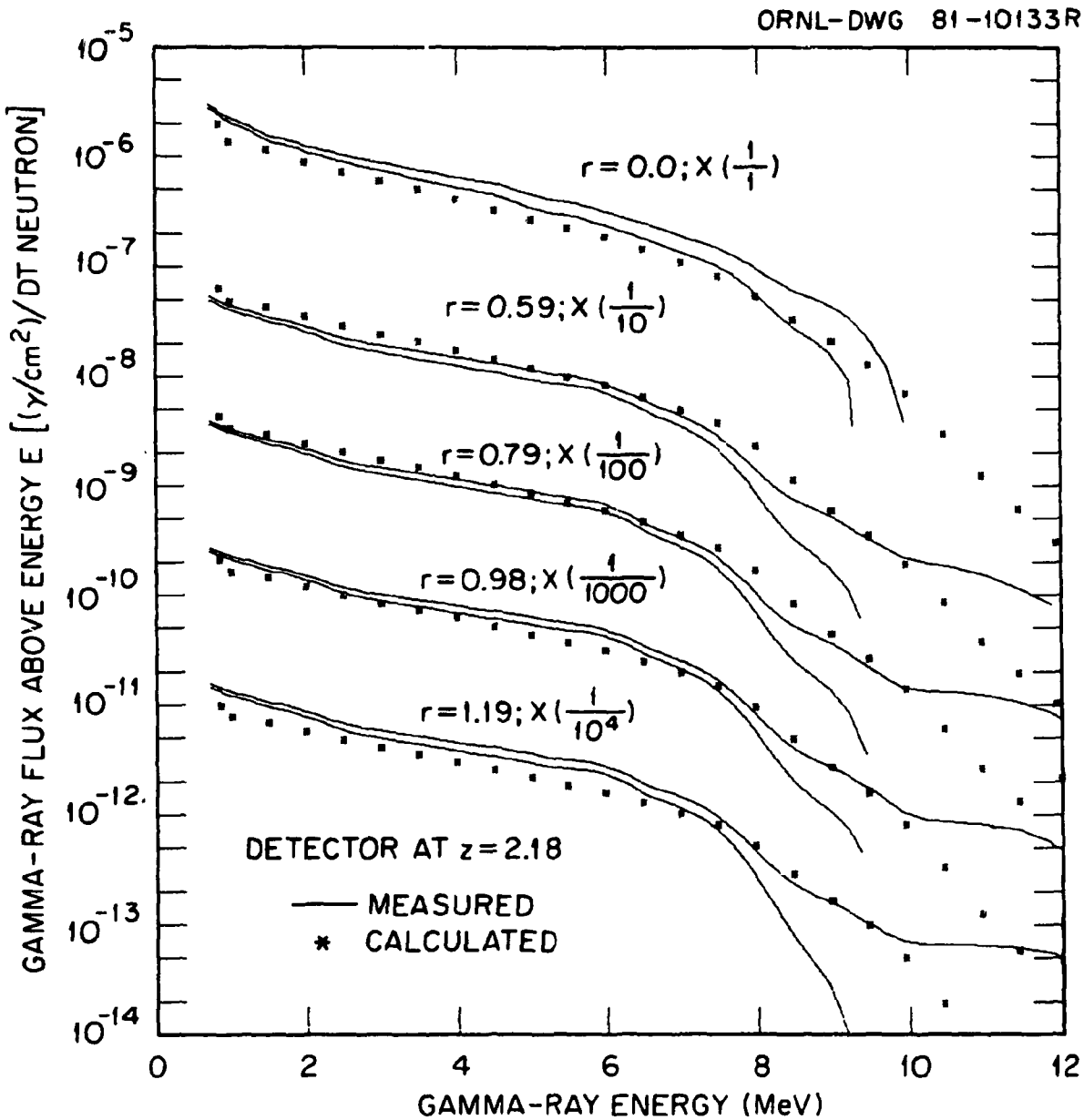


Fig. 26. Gamma ray flux above energy E versus gamma ray energy for the detectors at z = 2.08 m; r = 0.0, 0.59, 0.79, 0.98, and 1.19 m.

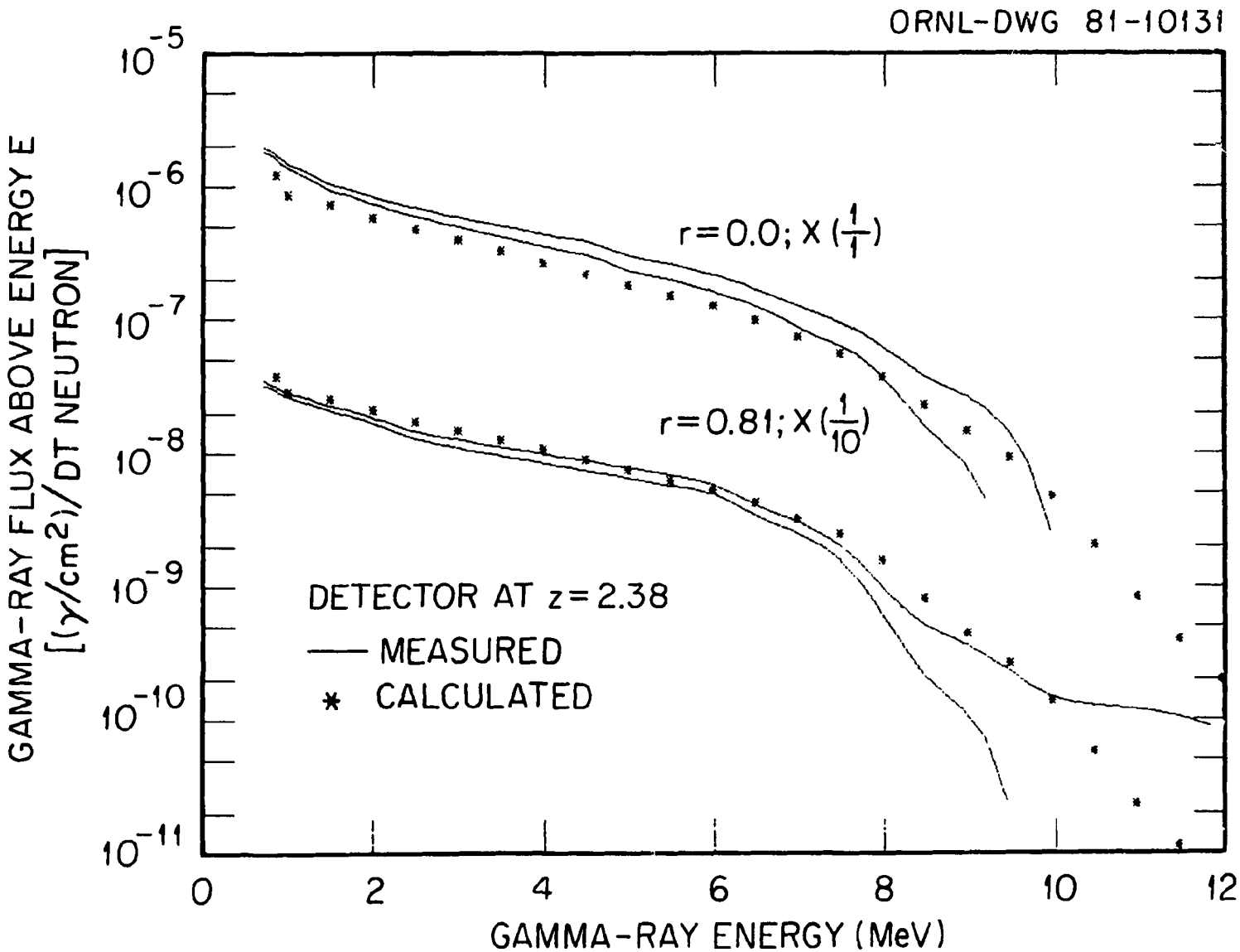


Fig. 27. Gamma ray flux above energy E versus gamma ray energy for the detectors at z = 2.38 m; r = 0.0 and 0.81 m.

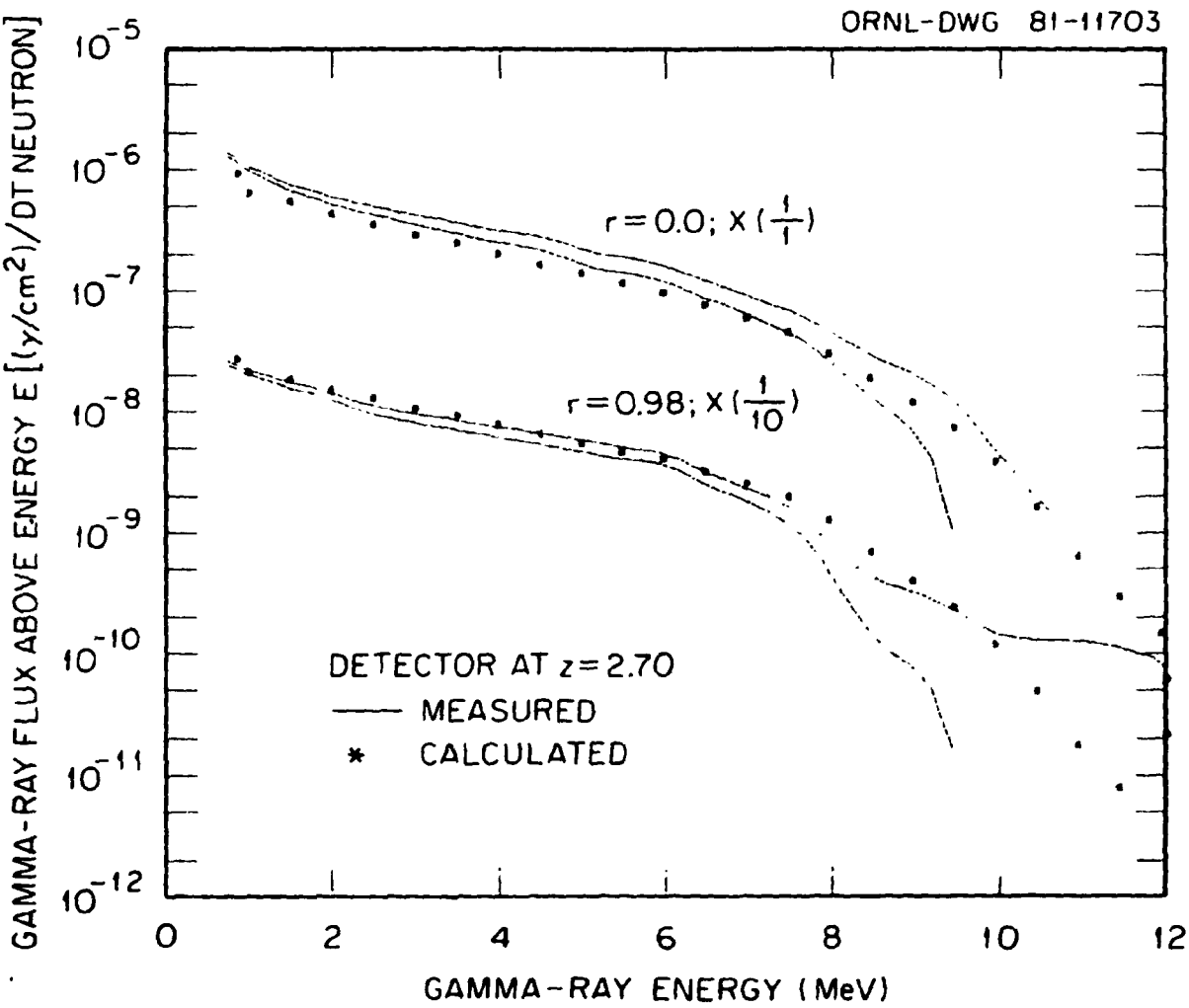


Fig. 28. Gamma ray flux above energy E versus gamma ray energy for the detectors at z = 2.70 m; r = 0.0 and 0.98 m.

polynomial expansion. The calculation generally reproduces the measurements in magnitude but because of the rather coarse energy group structure, the various peaks in the measured differential distributions are not reproduced. The important point to note in these comparisons is that the gamma rays that contribute to these spectra are due, in large part, to the reactions of low energy neutrons (<850 keV) in the experimental components. Although the neutron spectra are compared for energies greater than 850 keV, the radiation transport calculation was completed for neutrons down to thermal energies. Correspondingly, some of the gamma rays appearing in the distributions are due to thermal neutron capture reactions and these photons are accounted for in the calculation.

## V. SUMMARY

The results obtained here suggest that ∿14 MeV neutron streaming through the ducts and other penetrations in the blanket-shield assemblies of fusion reactors will require careful treatment of the energetic (>10 MeV) neutron elastic and inelastic scattering from the duct material. Although the duct geometry and neutron source considered here are simpler than in a reactor, the impact on the calculated neutron spectra of the forward peaked single scattering is sufficiently large to warrant a careful treatment in the analysis of neutron streaming.

The apparent requirement for representing the forward peaked neutron elastic and inelastic single scattering angular distributions with high order Legendre polynomial expansions may preclude the use of discrete ordinates or Monte Carlo radiation transport methods that require multigroup cross section data. Even if it were possible to obtain the cross section data with high order expansions of the angular distributions, the

computer core storage and running time requirements would be prohibitive. The utilization of transport codes that use continuous cross section data or the networking of transport codes that use both multigroup and continuous cross sections, as was developed for this study, may represent the only feasible approach for analysis of radiation streaming.

## REFERENCES


1. R. T. Santoro, R. A. Lillie, R. G. Alsmiller, Jr., J. M. Barnes, "Two- and Three-Dimensional Neutronics Calculations for the Tokamak Fusion Test Reactor," Nucl. Sci. Eng. 70, 225-242 (1979).
2. R. T. Santoro, J. S. Tang, R. G. Alsmiller, Jr., J. M. Barnes, "Monte Carlo Analysis of the Effects of a Blanket-Shield Penetration on the Performance of a Tokamak Fusion Reactor," Nucl. Technol. 37, 65-72 (1978).
3. M. A. Abdou, L. J. Milton, J. C. Jung and E. M. Gebhard, "Multi-dimensional Neutronics Analysis of Major Penetrations in Tokamaks," Proc. 2nd Top. Mtg. Technology of Controlled Nuclear Fusion, Richland, WA, Sept. 21-23, 1975, Vol. I, p. 845.
4. W. T. Urban, T. J. Seed, D. J. Dudziak, "Nucleonic Analysis of a Preliminary Design for the ETF Neutral Beam Injector Duct Shielding," 4th Top. Mtg. on the Technology of Controlled Nuclear Fusion, Oct. 14-17, 1980, King of Prussia, PA (to be published in the Proceedings).
5. R. A. Lillie, R. T. Santoro, R. G. Alsmiller, Jr., J. M. Barnes, "Neutron and Gamma Ray Streaming Calculations for the ETF Neutral Beam Injectors," ORNL/TM-7705, Oak Ridge National Laboratory (1981).
6. Y. Seki, H. Iida, R. T. Santoro, H. Kawasaki, M. Yamauchi, "Radiation Streaming Calculations for INTOR-J," Trans. Am. Nucl. Soc. 38, 555 (1981).
7. M. A. Abdou, Y. Gohar, J. C. Jung, "Radiation Shielding of Major Penetrations in Tokamak Fusion Reactors," Trans. Am. Nucl. Soc. 38, 553 (1981)

References (Cont'd)

8. R. T. Santoro, R. G. Alsmiller, Jr., J. M. Barnes, G. T. Chapman, "Calculation of Neutron and Gamma-Ray Energy Spectra for Fusion Reactor Shield Design: Comparison With Experiment," Nucl. Sci. Eng. 78, 259 (1981).

9. R. T. Santoro, J. M. Barnes, R. G. Alsmiller, Jr., E. M. Oblow, "Calculational Procedures for the Analysis of Integral Experiments for Fusion Reactor Design: Attenuation Experiments," ORNL-5777, Oak Ridge National Laboratory (1981).

10. W. R. Burrus and V. V. Verbinski, Nucl. Instrum. Methods 67, 181 (1979).

11. G. T. Chapman, G. L. Morgan and J. W. McConnell, "The ORNL Integral Experiments to Provide Data for Evaluating MFE Shielding Concepts. Part I: Attenuation Measurements," ORNL/TM-7356, Oak Ridge National Laboratory (to be published).

12. G. T. Chapman, G. L. Morgan, J. W. McConnell, "The Use of a Small Accelerator as a Source of 14-MeV Neutrons for Shielding Studies," presented at the Sixth Conference on the Applications of Accelerators in Research and Industry, North Texas State University, Denton, Texas, Nov. 3-5, 1980, and published in the Proceedings.

13. R. W. Roussin, C. R. Weisbin, J. E. White, N. M. Greene, R. Q. Wright, J. B. Wright, "The CTR Processed Multigroup Cross Section Library for Neutronics Studies," ORNL/RSIC-37, Radiation Shielding Information Center, Oak Ridge National Laboratory (1975); also available as DLC-41.

References (Cont'd)

14. W. W. Engle, Jr., "A User's Manual for ANISN, A One-Dimensional Discrete Ordinates Code with Anisotropic Scattering," K-1693, Oak Ridge National Laboratory (1967).

15. "BUGLE, Coupled 45-Neutron, 16-Gamma-Ray, $P_3$, Cross Sections for Studies by the ANS 6.1.2 Shielding Standards Working Group on Multigroup Cross Sections," DLC-47 Radiation Shielding Information Center, Oak Ridge National Laboratory (1977).

16. N. M. Greene et al., "AMPX: A Modular Code System for Generating Coupled Multigroup Neutron-Gamma Libraries from ENDF/B," ORNL/TM-3706, Oak Ridge National Laboratory (1976).

17. R. A. Lillie, R. G. Alsmiller, Jr. and J. T. Mihalczo, Nucl. Technol. 43, 373-381 (1979).

18. W. A. Rhoades and F. R. Mynatt, "The DOT III Two-Dimensional Discrete Ordinates Radiation Transport Code," ORNL/TM-4280, Oak Ridge National Laboratory (1979).

19. "FALSTF, Informal Notes," CCC-351, Radiation Shielding Information Center, Oak Ridge National Laboratory (1979).

20. M. B. Emmett, "The MORSE Monte Carlo Radiation Transport Code System," ORNL-4972, Oak Ridge National Laboratory (1975).

21. M. M. Wadel, Jr., "PXMORSE, A Continuous Energy Monte Carlo Code," Ph.D. Thesis, University of Tennessee (1981).